Nanoscale

REVIEW

View Article Online
View Journal | View Issue

Check for updates

Cite this: *Nanoscale*, 2025, **17**, 23228

Specific detectivity-oriented low-noise management in organic photodetectors

Seungjae Hong, Tae Hyuk Kim, Seunghyun Oh and Jae Won Shim *

The need to detect faint light signals with unparalleled precision is redefining organic photodetectors (OPDs) and unlocking their transformative applications in biosignal monitoring, optical communication, and quantum-level photodetection. The specific detectivity (D^*) is an essential metric in such scenarios that captures the ability of an OPD to extract weak signals from noise and is a function of the active area, bandwidth, and noise-equivalent power of the device. This review reframes the pursuit of an ultrahigh D^* by targeting noise current suppression, —a formidable issue in which shot, thermal, flicker, and generation-recombination noise sources combine to obscure signals. First, the complexities of noise are discussed, then various strategies for addressing its causes are explored in terms of charge injection, interfacial traps, and material defects. These strategies include: precisely tailoring active layers to mitigate trap-assisted recombination and charge generation, selectively optimizing transport layers to mitigate interfacial defects at the electrode interface and block unwanted injection currents, and applying architectural innovations such as tandem and nanostructured designs that transcend single-junction paradigms. By combining mechanism-driven insights with a critical appraisal of current frontiers, this review highlights untapped opportunities and promising strategies for developing OPDs with unprecedented sensitivity and performance.

Received 30th June 2025,
Accepted 17th September 2025

DOI: 10.1039/d5nr02756j

rsc.li/nanoscale

Published on 18 September 2025. Downloaded on 16.05.26 11:55:54.

1 Introduction

Advances in next-generation technologies such as biosignal monitoring, optical communication, and photonic sensing have steadily increased demand for high-performance photodetectors.[1–5] Although inorganic crystalline materials (*e.g.*, Si and Ge) are typically used in these sensing technologies, their rigid structures, complex fabrication processes, and limited spectral tunability limit the broader application of photodetectors incorporating these materials.[6,7] Notably, organic photodetectors (OPDs) possess distinct material properties that overcome these limitations, facilitating tailored spectral responses, compatibility with flexible/stretchable substrates, and simplified integration into target applications.[8–14] However, the commercial viability of OPDs is hindered by their relatively high intrinsic noise levels compared to their inorganic counterparts, as advanced applications under challenging conditions require the precise detection of faint optical signals that can be readily overshadowed by excessive noise.[15]

The key metrics for evaluating the performance of OPDs include responsivity (R), cut-off frequency, dark current density, and specific detectivity (D^*). R is defined as the ratio of output photocurrent to incident optical power and serves as a measure of the device's photo-to-electrical conversion efficiency. The cut-off frequency (−3 dB frequency) is the frequency at which the output amplitude decreases to 70.8%, representing the bandwidth of the device. Dark current refers to the current that flows through the device in the absence of illumination, and when normalized by the device area, it is expressed as dark current density. The detailed mechanisms underlying dark current are illustrated in Fig. 1. First, in the absence of traps, the dark saturation current J_0 follows a thermal generation mechanism determined by the effective gap E_{CT}. In addition, Shockley–Read–Hall (SRH) generation, in which trap states mediate electron–hole pair generation, gives rise to a larger magnitude of dark current. Finally, under strong electric fields, the Poole–Frenkel effect facilitates thermal emission of carriers trapped at defect sites, satisfying both the magnitude and field dependence, which together converge with the experimentally observed dark current density. D^* is arguably the most critical metric in assessing the performance of a photodetector. Defined by the equation:

$$D^* = \frac{\sqrt{A_{PD} \cdot \Delta f}}{NEP} (\text{cm Hz}^{1/2} \text{W}^{-1} \text{ or Jones}) \quad (1)$$

where NEP denotes the noise-equivalent power (the optical power at which the signal current equals the noise

School of Electrical Engineering, Korea University, Seoul 02841, Republic of Korea. E-mail: jwshim19@korea.ac.kr

This journal is © The Royal Society of Chemistry 2025

Published on 18 September 2025. Downloaded on 16.05.26 11:55:54.

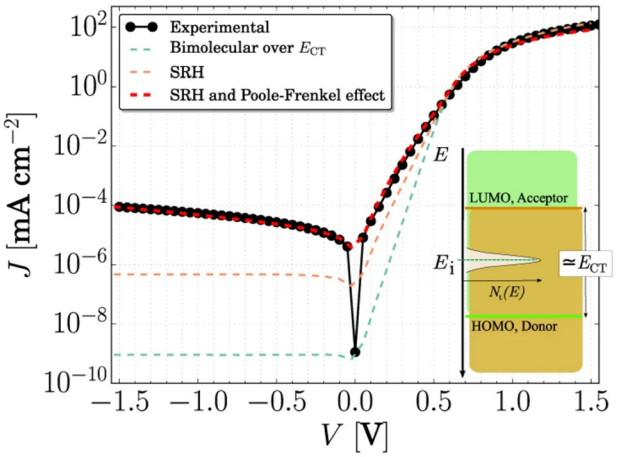

Fig. 1 Simulated J–V characteristics for a device. The graph compares simulated data (dashed lines) with experimental results (symbols and solid lines). Also shown are the J–V characteristics for the Shockley–Read–Hall (SRH) process without the Poole–Frenkel effect, and for bimolecular generation over the charge-transfer state energy (E_{CT}). Inset: a schematic diagram illustrating the mid-gap trap distribution within the donor-acceptor energy system. Reprinted with permission from ref. 84.

current),[16,17] A_{PD} is the active area of the device, and Δf is the bandwidth, D^* quantitatively characterizes the capability of a photodetector to distinguish weak optical signals from its device-intrinsic noise.[18–20] Although an accurate determination of D^* requires the precise measurement of NEP owing to changes in R when the illumination is beyond the linear dynamic range of the photodetector, assuming that the device maintains linear photocurrent generation at NEP-level illumination, D^* can be approximated as:

$$D^* \approx \frac{R\sqrt{A_{PD} \cdot \Delta f}}{i_n} \quad (2)$$

where i_n is the total noise current.[21,22] Thus, D^* can be improved by either increasing R or decreasing i_n.

Table 1 summarizes the key performance metrics of OPDs reported in recent studies, including D^*, dark current density, external quantum efficiency (EQE), NEP, and active layer thickness, along with their corresponding measurement conditions. Note that shot-noise-based D^* is calculated under the assumption that shot noise is the dominant component of the total noise, with the influence of thermal, flicker, and generation–recombination noise reduced, and therefore it may be overestimated compared to the actual value. Active layer thickness is one of the critical parameters influencing the dark current of the device. A thicker active layer increases the carrier transport distance, thereby raising the probability of carrier recombination within the layer. As a result, charge extraction under dark conditions is reduced, leading to lower dark current. This demonstrates that thickness is not merely a structural parameter but an essential mechanism directly related to noise suppression and detectivity enhancement.

As expressed in the above equation, D^* is normalized with respect to device area and measurement frequency. Therefore, an accurate understanding of these two parameters is essential for proper interpretation of D^* and for ensuring objective performance comparisons across different studies. Paradoxically, despite this normalization being intended to minimize the

Table 1 Key performance metrics of high-performance OPDs in recent studies. The noise spectral density-based D^* and the shot-noise-limited D^* were calculated using the equations $D^* = \frac{R\sqrt{A}}{S_n}$ and $D^* = \frac{R}{\sqrt{2qJ_d}}$, respectively

D^* (Jones)	EQE (%)	J_d (A cm^{-2})	NEP (W or W Hz$^{-1/2}$)	Active layer thickness (nm)	Ref.
1.71 × 10^{13} (noise current based, 1100 nm, 0 V)	**58.9** (1100 nm, 0 V)	**4.15 × 10^{-8}** (−0.1 V)	**2.56 × 10^{-14} W** (1070 nm)	**110**	135
1.40 × 10^{14} (shot noise based, 950 nm, 0 V)	**48.3** (950 nm, 0 V)	**2.26 × 10^{-11}** (0 V)	—	—	136
3.72 × 10^{13} (noise spectral density based (averaged), 1060 nm, −0.1 V)	**41.6** (1060 nm, 0 V)	**2.61 × 10^{-10}** (−0.1 V)	—	**270**	137
2.93 × 10^{12} (noise spectral density based (10 Hz), 870 nm, 0 V)	**68.4** (870 nm, 0 V)	**1.70 × 10^{-10}** (0 V)	—	**130**	138
3.45 × 10^{13} (shot noise based, 620 nm, −1 V)	**65.0** (620 nm, 0 V)	**3.63 × 10^{-10}** (−1 V)	**9.07 × 10^{-15} W Hz$^{-1/2}$** (~ 670 nm)	**150**	139
3.02 × 10^{12} (noise current based, 790 nm, −2 V)	**59.6** (770 nm, −2 V)	**1.65 × 10^{-9}** (−2 V)	—	**100**	140
7.35 × 10^{13} (shot noise based, 805 nm, −0.2 V)	**75.3** (805 nm, −0.2 V)	**1.38 × 10^{-10}** (−0.2 V)	—	**180**	141
4.65 × 10^{13} (shot noise based, 880 nm, 0 V)	**52.4** (880 nm, 0 V)	**2.01 × 10^{-10}** (0 V)	—	**180–195**	142
7.89 × 10^{12} (noise spectral density based (1 kHz), 900 nm, 0 V)	**83.6** (~900 nm, 0 V)	**4.65 × 10^{-10}** (0 V)	**2.55 × 10^{-14} W Hz$^{-1/2}$** (900 nm)	**120**	143
2.8 × 10^{12} (noise spectral density based (10 kHz), 840 nm, −0.1 V)	**16.3** (840 nm, −0.1 V)	**3.70 × 10^{-10}** (−0.1 V)	—	—	144
1.04 × 10^{13} (noise spectral density based (10 Hz), 800 nm, 0 V)	**66.7** (800 nm, 0 V)	**1.75 × 10^{-10}** (0 V)	**< 10^{-13} W Hz$^{-1/2}$** (400–860 nm)	—	145
>10^{12} (shot noise based, 1300 nm, 0 V)	**26.0** (1100 nm, 0 V)	**2.40 × 10^{-10}** (0 V)	—	—	146
1.40 × 10^{13} (noise spectral density based (10 Hz), 930 nm, 0 V)	**33.5** (1000 nm, 0 V)	**5.3 × 10^{-11}** (0 V)	—	**110**	147
3.81 × 10^{12} (noise spectral density based (10 Hz), 1100 nm, 0 V)	**18.9** (1100 nm, 0 V)	**3.58 × 10^{-10}** (0 V)	**6.12 × 10^{-14} W** (1100 nm)	—	148

Published on 18 September 2025. Downloaded on 16.05.26 11:55:54.

influence of device area, large-area OPDs used in applications such as digital X-ray imaging and document scanners often suffer from increased fabrication complexity and higher defect densities, which induce shunt pathway formation. This in turn amplifies noise, reduces D^*, and complicates objective comparison of detectivity across devices of different sizes. To properly evaluate D^* in large-area OPDs, it is first necessary to recognize that the probability of intrinsic material and physical defects increases with active area, thereby raising the dark current floor, and to incorporate this understanding into the quantitative assessment of D^*. In this review, we instead place deliberate emphasis on miniaturized OPDs, where reducing the photosensitive area minimizes leakage current and parasitic capacitance, thereby enabling high detectivity under low-light conditions, and we examine performance improvement strategies aimed at advancing next-generation technologies such as high-resolution imaging and biomedical sensors. Moreover, reporting high D^* values based on NEP estimated within a narrow measurement bandwidth of around 1 Hz does not faithfully reflect the conditions required for practical applications (typically in the kHz to tens of kHz range) and thus carries the limitation of overestimating detectivity. However, for ultra-sensitive OPDs operating at NEP levels below the pW regime, there exists a practical limitation in that the actual usable bandwidth cannot be readily specified due to the intrinsic constraints of current measurement instruments. To suppress the noise floor of the measurement system itself, it becomes necessary to adopt a narrow measurement bandwidth, which in this context functions as an aperture in the frequency domain, allowing the desired signal to be captured with high precision. For this reason, prior works have adopted narrow measurement bandwidths and reported NEP and D^* accordingly. Therefore, for accurate and objective evaluation of NEP and D^*, a clear understanding of the measurement frequency conditions must be established, and subsequent studies should adopt improved practices by reporting device performance across the maximum measurable bandwidth of the system.

Strategies for increasing R aim to promote efficient exciton dissociation and rapid charge extraction. Some methods improve the energetic alignment of adjacent functional layers or increase the crystallinity of the active layer to enhance charge transport;[23,24] other methods introduce additional dopants or intentionally form trap states to enable photomultiplication through gain mechanisms.[25,26] However, the improvements realized using such methods often occur at the expense of elevated noise, which can potentially reduce D^*.[27]

Therefore, noise suppression can provide a more effective approach for enhancing D^*. Reducing i_n directly improves the signal-to-noise ratio (SNR), thereby increasing sensitivity to weak optical signals.[28,29] Consistent with the R-in trade-off, some noise reduction methods, including the introduction of additional functional layers, may decrease R.[30,31] However, a substantial decrease in noise often outweighs the moderate loss of R, ultimately improving D^*. Moreover, certain noise reduction techniques, including trap passivation and interfacial morphology refinement, can maintain or even enhance R, thereby achieving the dual benefits associated with reducing i_n and increasing R.[32,33] These strategies also improve environmental- and photo-stability, offering critical advantages for precision-demanding applications, such as biosensing, nueromorphic imaging, and high-resolution spectroscopy, in which the high-fidelity detection of low-intensity signals is crucial.[34,35] When coupled with the inherent bandgap tunability of organic semiconductors, providing noise suppression in OPDs can realize highly customizable spectral responses ranging from the ultraviolet (UV) to shortwave infrared (SWIR) regions. Thus, the synergistic combination of effective noise management and molecular engineering flexibility makes noise suppression a universally robust and scalable approach for increasing D^*.

A comprehensive understanding of the physical origin of noise is imperative for rationally designing low-noise OPDs. The total noise current in an OPD originates from a combination of various intrinsic sources. Intrinsic noise mechanisms include shot noise, thermal (Johnson–Nyquist) noise, flicker noise ($1/f$ noise), and generation–recombination (g–r) noise, each governed by distinct frequency dependencies and underlying transport phenomena.

Shot noise originates from the discrete and stochastic transport of charge carriers. Its statistical behavior is effectively described by the Poisson distribution,[36–39] and its magnitude can be approximated by

$$I_{\text{shot}} = \sqrt{2qI_D\Delta f} \tag{3}$$

where q is the elementary charge, I_D is the dark current and Δf is the measurement bandwidth.[18] Note that this equation indicates that shot noise increases proportionally with the square root of both the dark current and the bandwidth. Thermal noise is attributed to the thermally induced agitation of carriers within the resistive elements of the device.[16,40] It is typically expressed as:

$$I_{\text{thermal}} = \sqrt{4k_BT\Delta f/R_{sh}} \tag{4}$$

where k_B is the Boltzmann constant, T is the absolute temperature, and R_{sh} is the shunt resistance.[41] The sum of I_{shot} and I_{thermal} constitutes the frequency-independent white noise as follows:[42]

$$I_{\text{white}} = \sqrt{I_{\text{shot}}^2 + I_{\text{thermal}}^2} \tag{5}$$

In contrast, flicker noise is characterized by its inverse dependence on frequency (*i.e.*, $1/f$) and prominence at low frequencies; it is commonly associated with charge trapping and detrapping phenomena, which typically occur at interfaces or within disordered regions of the active layer.[43,44] Although the precise physical origin of flicker noise remains under active investigation, it is often indicative of material inhomogeneities or interface instability.[45] Lastly, g–r noise arises from the random transitions of carriers between localized trap states and extended band states, which produce fluctuations in carrier density while preserving overall charge neutrality; its

 This journal is © The Royal Society of Chemistry 2025

Published on 18 September 2025. Downloaded on 16.05.26 11:55:54.

power spectral density typically scales with $1/f^2$.[46–48] This noise is particularly relevant in materials exhibiting high trap densities or pronounced energetic disorder, where its spectral signature typically appears in Lorentzian form.[49,50] The current fluctuation due to g–r noise is often modeled as

$$i_{g-r} = \sqrt{2NqI_{ph}} \quad (6)$$

where N is a prefactor that depends on the recombination kinetics and conductive properties of the active material, and I_{ph} is the generated photocurrent.[51]

Given the various advantages of reducing the total noise floor, this review focuses on strategies for suppressing white noise through dark current reduction and maximization of shunt resistance, and mitigating low-frequency noise *via* trap

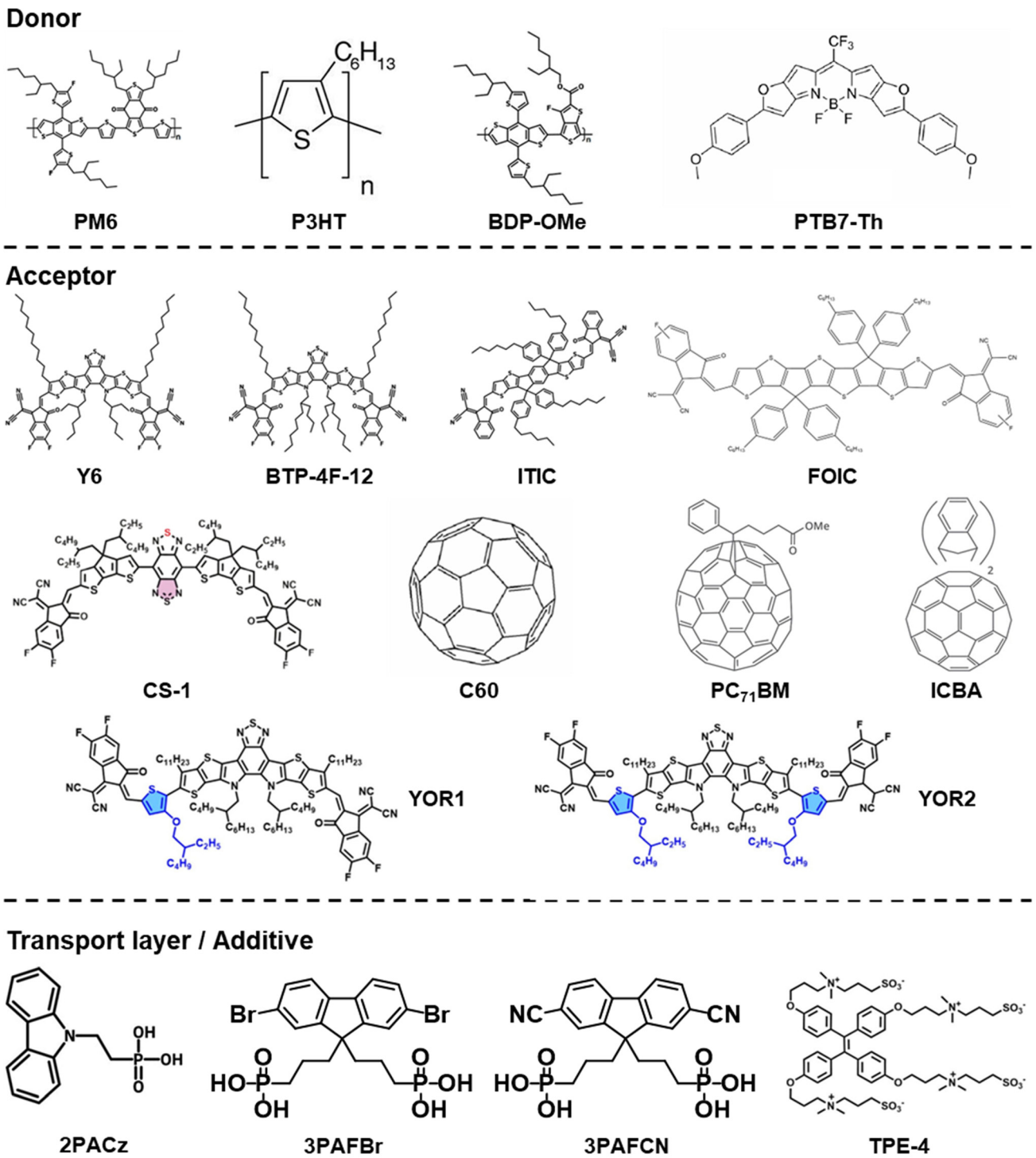

Fig. 2 Chemical structures of the donor, acceptor, transport layer, and additive materials discussed in this study.

Published on 18 September 2025. Downloaded on 16.05.26 11:55:54.

density minimization, thereby addressing all of the major noise components discussed above. The subsequent sections explore several approaches for noise current reduction: active layer engineering to suppress trap-assisted transport, transport layer modification to minimize injection leakage, and advanced device architectures such as tandem stacks and noise-suppression-based photomultiplication-type OPDs. The chemical structures of the donor, acceptor, transport layer, and additive materials introduced in this study are presented in Fig. 2. By addressing the root causes of noise rather than merely amplifying the signal output, these methodologies offer a path for realizing intrinsically superior OPDs that exhibit high detectivity, spectral uniformity, and operational robustness under real-world conditions.

2 Active layer engineering for noise reduction

The active layer is the core component of an OPD responsible for photon absorption, charge generation, and carrier transport.[52–54] Limitations on the interfacial properties of this layer, which include the presence of trap states, structural imperfections, morphological disorder, and misaligned energy levels, significantly influence the magnitude of the intrinsic noise currents within.[55] These limitations have been recently addressed through efforts focusing on compositional control, morphological optimization, fine-tuning fabrication procedures, and incorporating functional additives to suppress noise arising from unwanted charge injection and parasitic leakage pathways.[56–64] This section presents advanced design guidelines that have been developed to enhance the performance ceiling of OPDs accordingly.

Labanti *et al.* demonstrated the effective suppression of dark current by deliberately reducing the crystallinity of the bulk heterojunction (BHJ) *via* acceptor component dilution.[65] Non-fullerene acceptors that typically exhibit high crystallinity, such as Y6, facilitate the formation of continuous carrier transport pathways through their pronounced π–π stacking and quadrupolar intermolecular interactions.[66–68] Decreasing the acceptor concentration disrupts the crystalline ordering and modifies the film morphology, thereby interrupting the electron percolation pathways. In addition, this approach leverages a field-dependent charge separation mechanism to suppress the generation of unwanted photocurrents. Fig. 3a presents a schematic illustrating excited-state delocalization and the resulting charge generation in both balanced and diluted blends. In the balanced blend, distinct neat crystalline Y6 domains are formed due to the strong π–π stacking of Y6 and its high quadrupole moment. This leads to delocalized excited states with low binding energy, which facilitate exciton dissociation and, in turn, result in charge generation even under dark conditions, thereby increasing dark current. In contrast, in the diluted blend, the crystallinity and intermolecular interactions of Y6 are disrupted by the higher concentration of PM6, leading to the formation of small, isolated Y6 domains. These domains support localized, emissive states with higher binding energy, which hinder exciton dissociation and suppress thermal charge generation, a major contributor to dark current. Consequently, this approach effectively suppresses shot noise, the most dominant component of the noise floor, and significantly enhances D^*.

In addition to conventional deposition methods, such as spin-coating and spray-coating (which are widely employed in solution-processed organic photodetectors), transfer printing techniques can be applied to facilitate additional layer design and thereby enhance the interfacial quality and suppress charge injection while reducing noise.[69,70] He *et al.* developed a novel hybrid BHJ-planar heterojunction (PHJ) architecture, named B-PHJ, by applying an ultra-thin PM6 donor barrier layer on a BHJ active layer *via* water transfer printing.[71] This laminated PM6 layer formed a van der Waals interface that mitigated the interfacial traps commonly associated with dangling bonds arising from molecular contacts in traditional MoO_3 thermal evaporation processes. Fig. 3b illustrates two key mechanisms for reducing dark current in the B-PHJ structure through an energy band diagram. First, an appropriate energy offset is established between the LUMO level of PM6 and the Ag electrode, which acts as a high-energy barrier that prevents electron injection from the electrode into the active layer, thereby suppressing reverse injection current. Second, the water transfer printing method forms a high-quality van der Waals interface that decreases the trap density at the interface and reduces thermal generation current arising from traps. Together, these mechanisms lead to a reduction in dark current, which consequently lowers shot noise and contributes to an overall decrease in the noise floor. As shown in Fig. 3c, an increase in the thickness of the PM6 layer led to a higher onset voltage for the space-charge-limited current (SCLC), indicating delayed charge injection under space-charge conditions.[72] Thus, the following expression for the corrected current density J_{corr} can be employed to eliminate the influence of series resistance R_s and R_{sh}:

$$J_{corr} = J - \frac{V_{rev} - J \times R_s}{R_{sh}} \quad (7)$$

where J is the absolute value of the apparent dark current density, V_{rev} are the absolute values of the applied reverse bias, the R_s and R_{sh} are the area-normalized series resistance and shunt resistance, respectively.[73] This relationship also explains the minimized dark current observed at an optimized barrier thickness of 24 nm. As a result, the dark current controlled by the high-energy barrier and the van der Waals interface leads to suppression of the shot noise floor, enabling the device to achieve a shot-noise-limited detectivity of $D^* = 3.68 \times 10^{14}$ Jones at 0 V and 850 nm. However, as previously noted, although this study acknowledges that shot noise is the dominant component among the noise sources and calculates D^* on this basis, it does not account for the full spectrum of noise contributions, and therefore the potential overestimation of D^* must be recognized. Jang *et al.* proposed an innovative A/BHJ device structure in which a BHJ layer is transfer-printed

 This journal is © The Royal Society of Chemistry 2025

Published on 18 September 2025. Downloaded on 16.05.26 11:55:54.

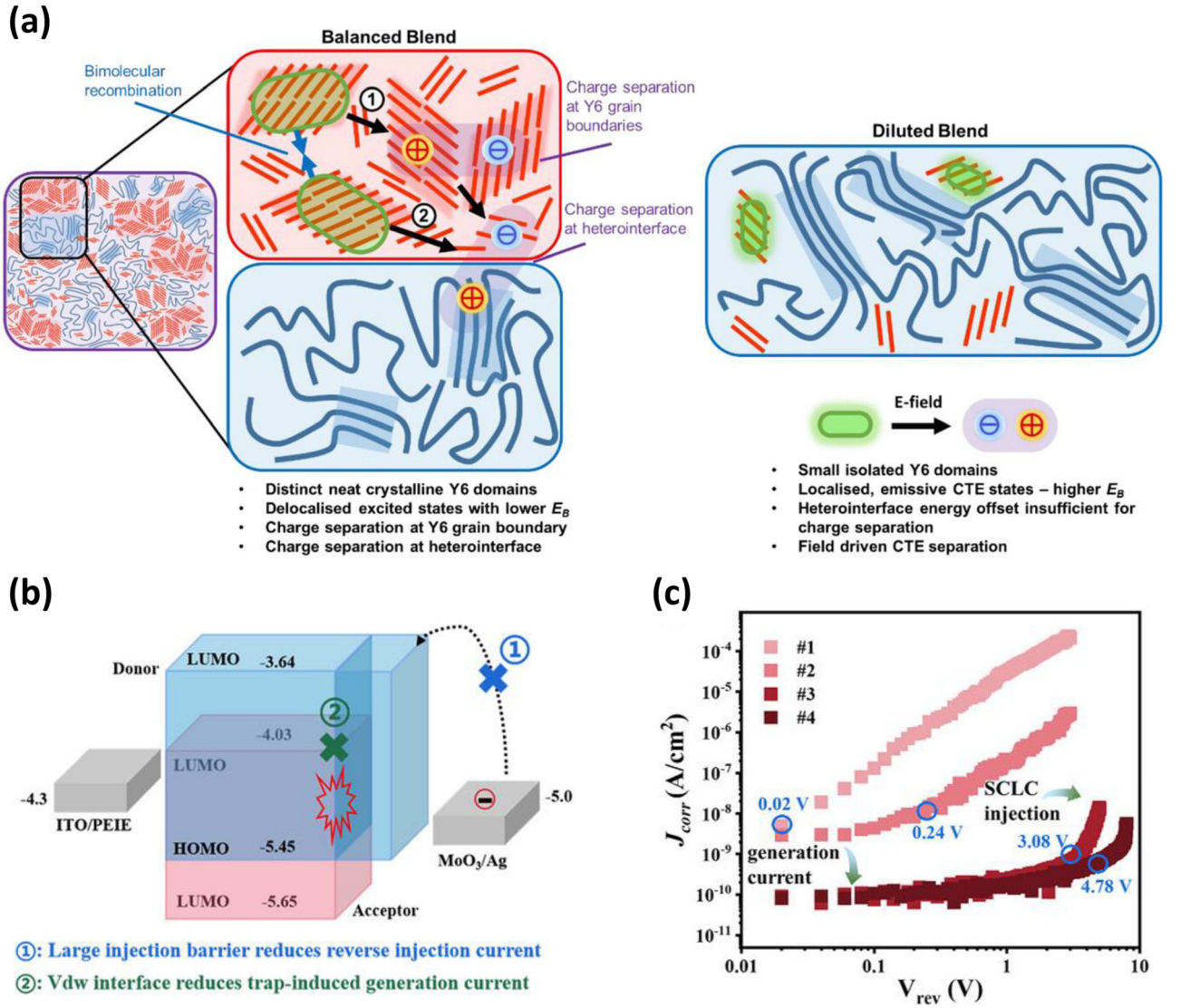

Fig. 3 (a) Charge generation in diluted and balanced blends. Schematic showing excited-state delocalization (green) and its effect on charge generation, with polymer chains (blue), Y6 molecules (red), and charge-separated states (purple); electrons and holes are indicated by negative and positive symbols. Reprinted with permission from ref. 65. (b) Dark-current reduction mechanism in the B-PHJ device. (c) Corrected current density-voltage curve of #1: w/o PM6 layer OPDs, #2: w/10 nm PM6 layer OPDs, #3: w/16 nm PM6 layer OPDs, #4: w/24 nm PM6 layer OPDs. Reprinted with permission from ref. 71. Copyright © 2025, Wiley-VCH.

onto a pre-formed single acceptor layer.[74] To do so, a polymer mold is synthesized by blending an aliphatic urethane diacrylate oligomer (EB 9270), 2-hydroxyethyl acrylate (HEA), and 1-hydroxycyclohexyl phenyl ketone (HCPK), then casting the mixture onto a silicon wafer and UV-curing it for 10 min. Next, the PM6:BTP-4F-12 blend solution is spin-coated onto the mold and annealed to form a solid-state BHJ layer. This solid BHJ film is transfer-printed onto a $PC_{71}BM$ acceptor layer, effectively preventing intermixing between adjacent layers and overcoming the long-standing issue of solvent nonorthogonality, which is inherent to solution-based spin-coating methods; this in turn realizes a reduction in trap density. Additionally, the $PC_{71}BM$ acceptor introduced between the indium tin oxide (ITO)/zinc oxide (ZnO) substrate and the BHJ layer forms a large injection barrier owing to its relatively deep highest occupied molecular orbital (HOMO) level, thereby blocking unwanted charge injection. These mechanisms allow the A–BHJ architecture to reduce the dark current on a fundamental level, thereby reducing shot noise, ultimately, this enhances the detectivity of the device.

Incorporating appropriate additives into the active layer has also emerged as an effective strategy for suppressing noise in OPDs. Lee *et al.* introduced molybdenum disulfide (MoS_2), a two-dimensional (2D) transition metal dichalcogenide (TMD), into a poly(3-hexylthiophene) (P3HT): indene-C_{60} bisadduct (ICBA) BHJ.[75] The inclusion of MoS_2 significantly mitigated Langevin recombination and reduced the trap density. Fig. 4a quantitatively illustrates the variations in the total and free

Published on 18 September 2025. Downloaded on 16.05.26 11:55:54.

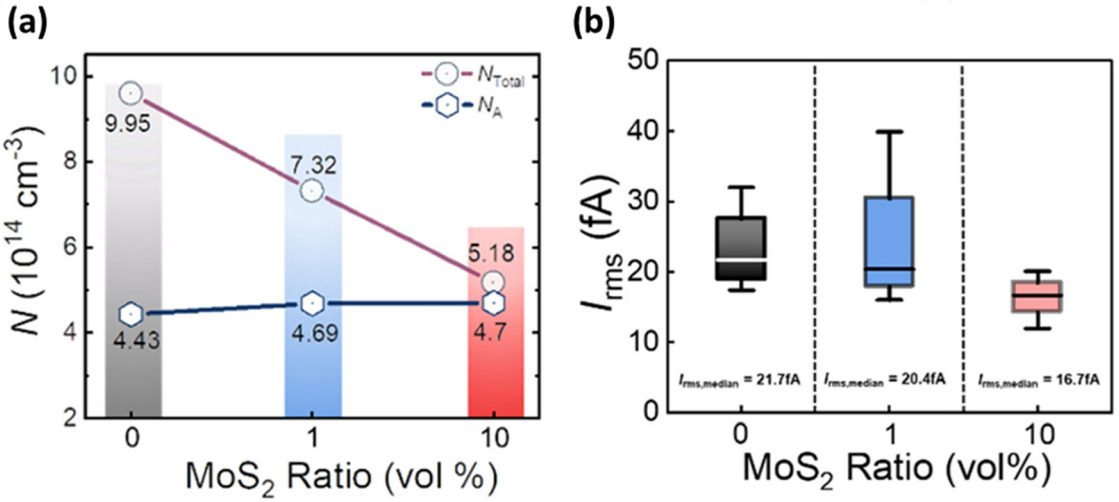

Fig. 4 (a) Comparison of total and free carrier densities among the three OPDs. (b) Averaged I_{rms} values from repeated measurements for three different OPD devices. Reprinted with permission from ref. 75. Copyright © 2025, American Chemical Society.

carrier densities with increasing MoS_2 concentration. At low frequencies (~1 kHz), both the trap states and free carriers responded to the AC signal, allowing the total carrier density to be estimated. By contrast, only free carriers contributed to the signal response at higher frequencies (~1 MHz) as the trap states were unable to follow the rapid signal modulation.[76] Although the free carrier density exhibited a slight increase with the addition of MoS_2, the total carrier density decreased markedly from 9.95×10^{14} cm^{-3} (without MoS_2) to 7.32×10^{14} cm^{-3} (with 1 vol% MoS_2), then decreased further to 5.18×10^{14} cm^{-3} at higher concentrations.[77,78] This trend confirms that the incorporation of MoS_2 facilitates the quantitative suppression of trap states, leading to a reduction in the total noise floor (Fig. 4b). According to eqn (2), this directly translates into an enhancement of D^*.

Near-infrared (NIR) and SWIR detection are critical applications of biological signal sensing, medical diagnostics, and flexible OPDs.[21,44,79,80] However, devices in these applications often suffer from high noise levels originating from thermal carrier generation in narrow-bandgap active layers.[81,82] Bills *et al.* proposed blending wide-bandgap insulating polymers with active matrices to overcome this limitation.[83] Various concentrations of non-conjugated insulating polymers such as polystyrene (PS), poly(methyl methacrylate) (PMMA), and polysulfone (PSU) were intercalated within the BHJ structure, diluting both the trap density and transport pathways, thereby effectively reducing the total noise current. Notably, the PSU-based ternary blend effectively reduced the number of trap states with energy levels near the mid-gap of the charge-transfer state, reducing the Shockley–Read–Hall (SRH) generation rate G, which can be expressed under a reverse bias as follows:

$$G = \frac{\beta_{SRH} N_t n_i}{2\cosh\left(\frac{E_t - E_i}{k_B T}\right)} \quad (8)$$

where β_{SRH} is the recombination rate constant, N_t is the trap state density, n_i is the intrinsic carrier concentration, E_i is the intrinsic Fermi level, and E_t is the trap energy level.[84] According to eqn (8), G increases as the trap energy approaches the mid-gap position. Therefore, shifting the trap states from energy levels near the mid-gap to deeper energy levels will reduce trap-assisted carrier generation. Although the presence of deep traps may hinder carrier collection at the electrodes, reducing R, the suppression of mid-gap traps has a more pronounced effect on the reduction of dark current, decreasing shot noise, lowering the noise floor across the entire frequency range, and enhancing the overall detectivity of the device. Cong *et al.* synthesized an ultra-narrow-bandgap acceptor, CS-1, based on an A–D–A_1–D–A architecture incorporating benzobisthiadiazole (BBT), and fabricated SWIR OPDs exhibiting high detectivity at 1300 nm.[85] The chemical structure of CS-1 is shown in Fig. 2. The central A_1 unit, BBT, possesses a strong electron-withdrawing nature, which enhances the intramolecular charge transfer (ICT) effect occurring between the donor and acceptor units. This strengthens electron π-delocalization, promotes intermolecular π–π stacking, reduces the bandgap, and lowers energetic disorder. The resulting reduction in disordered regions within the active layer suppresses carrier trapping–detrapping, thereby effectively mitigating flicker noise even in low-bandgap SWIR OPDs. In addition, the active layer morphology was improved by adopting a solution-dripping process in place of conventional spin-coating. Unlike the weak aggregation characteristics of the donor material PTB7-Th, CS-1 exhibits strong aggregation behavior. Spin-coating, due to slow film formation, induces excessive aggregation of CS-1, compromising film uniformity. In contrast, solution-dripping accelerates film formation, yielding smooth and uniform films. This results in continuous and homogeneous percolation pathways, which contribute to the overall reduction of noise (Fig. 5a). Consequently, detectivity estimated from rms white-noise

 This journal is © The Royal Society of Chemistry 2025

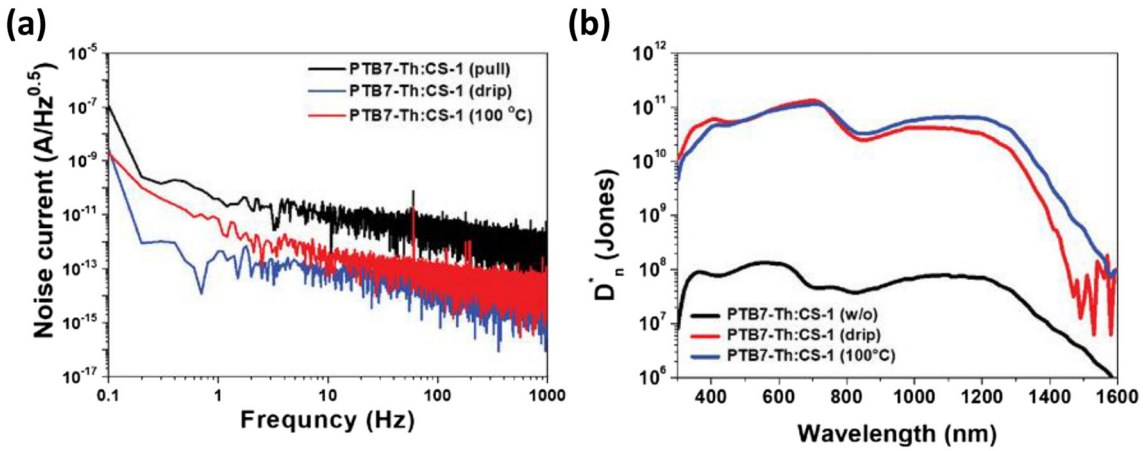

Fig. 5 (a) The zero-bias noise current spectrum and (b) corresponding detectivities of the PTB7-Th:CS-1 device under three different conditions. Reprinted with permission from ref. 85. Copyright © 2025, Wiley-VCH.

Published on 18 September 2025. Downloaded on 16.05.26 11:55:54.

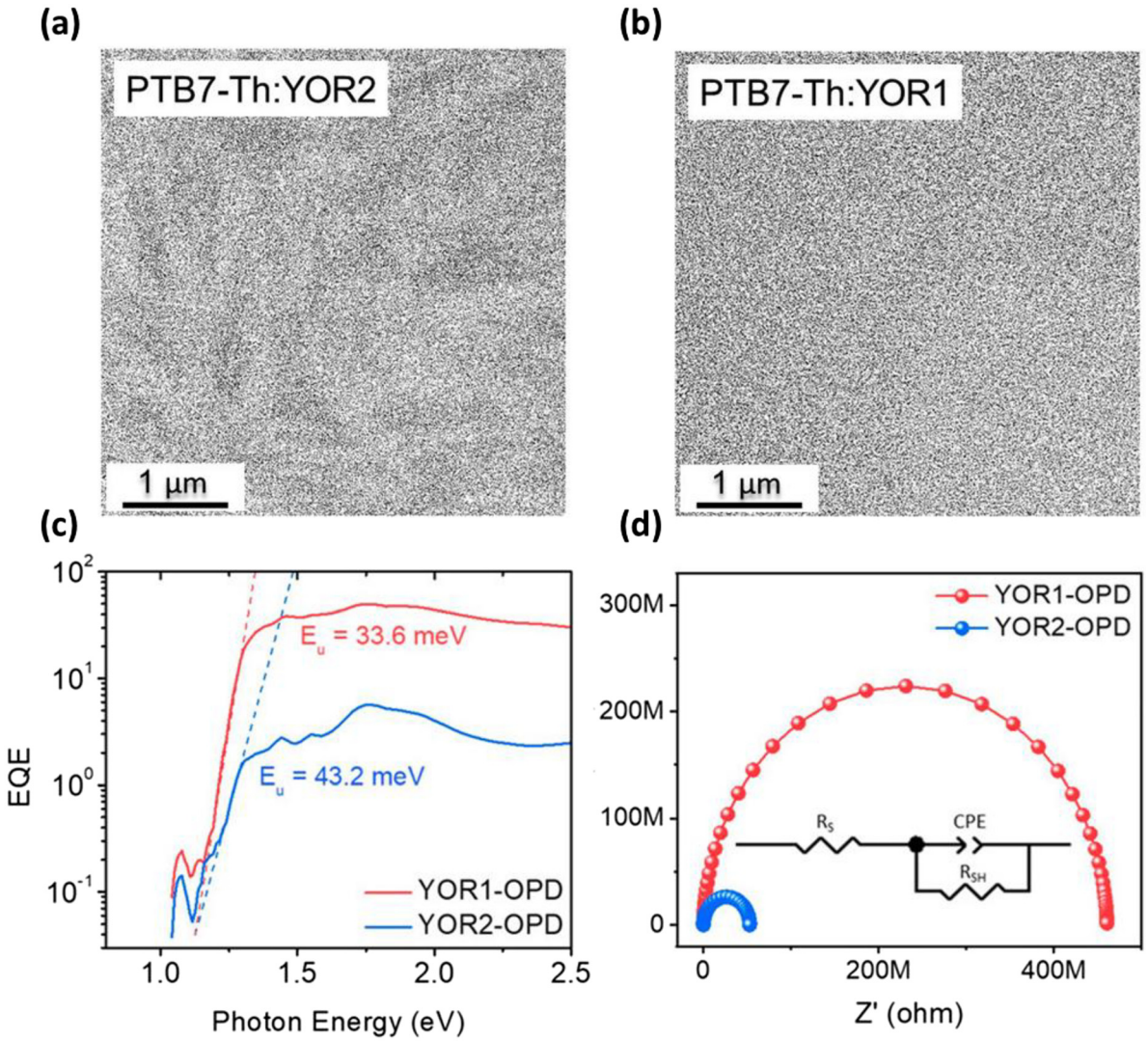

Fig. 6 Transmission electron microscopy images of the bulk heterojunction films of (a) PTB7-Th:YOR2 and (b) PTB7-Th:YOR1. (c) Urbach energy extracted from the long-wavelength tail of ln(EQE) for YOR1 and YOR2 OPDs. (d) Dark-condition electrochemical impedance spectra. Reprinted with permission from ref. 86. Copyright © 2023, American Chemical Society.

Published on 18 September 2025. Downloaded on 16.05.26 11:55:54.

current under a 0.1 Hz measurement bandwidth—although overestimated compared with D^* derived from experimentally measured NEP—achieved a high value of 2.96×10^{10} Jones at 1300 nm and 0 V (Fig. 5b). Ha *et al.* synthesized two new NFAs—2-((*Z*)-2-((5-(12,13-Bis(2-butyloctyl)-10-(((*Z*)-1-(dicyanomethylene)-5,6-difluoro-3-oxo-1,3-dihydro-2*H*-inden-2-ylidene)methyl)-3,9-diundecyl-12,13-dihydro-[1,2,5]thiadiaz-olo[3,4-*e*]thieno-[2″,3″:4′,5′]thieno[2′,3′:4,5]pyrrolo[3,2-*g*]thie no-[2′,3′:4,5]thieno[3,2-*b*]indol-2-yl)-4-((2-ethylhexyl)oxy)thio-phenn-2-yl)methylene)-5,6-difluoro-3-oxo-2,3-dihydro-1*H*-ind-en-1-ylidene)malononitrile (YOR1) and 2-((*Z*)-2-((5-(12,13-bis(2-butyloctyl)-10-(5-(((*Z*)-1-(dicyanomethylene)-5,6-difluoro-3-ox-*o*-1,3-dihydro-2*H*-inden-2-ylide-ne) methyl)-3-((2-ethylhexyl)ox y)thiophen-2-yl)-3,9-diundecyl-12,13-dihydro-[1,2,5]thiadiazol-*o*[3,4-*e*]thieno[2″,3″:4′,5′]thieno [2′,3′:4,5]pyrrolo[3,2 g]thieno [2′,3′:4,5]thieno[3,2-*b*]indol-2-yl)-4-((2-ethylhexyl)oxy)thiophe n-2-yl)methylene)-5,6-difluoro-3-oxo-2,3-dihydro-1*H*-inden-1-ylidene)malononitrile (YOR2)—to demonstrate the high potential of asymmetric NFAs in NIR OPDs.[86] A comparison of the chemical structures of YOR1 and YOR2 in Fig. 2 shows that the former adopts an asymmetric configuration, while the latter has a symmetric molecular structure. Due to stronger intermolecular interactions, YOR2 exhibits a pronounced tendency to self-aggregate, forming large and irregular fibrillar domains of approximately 550 nm (Fig. 6a). In contrast, the asymmetric nature of YOR1 minimizes excessive aggregation during donor blending, resulting in small crystallized domains of ~30 nm (Fig. 6b) and a reduced density of defects within the film. The relationship between superior nanoscale morphology and lower defect density is further supported by the EQE-derived Urbach energy in Fig. 6c. Compared with YOR2-OPDs (E_u = 43.2 meV), YOR1-OPDs exhibit a lower Urbach energy (E_u = 33.6 meV), which corresponds to reduced energetic disorder and a narrower width of localized states. This improvement is directly linked to higher shunt resistance (Fig. 6d), indicating suppression of thermal noise. As a result, YOR1-OPDs achieved a high D^* of 2.20×10^{11} Jones at 1000 nm (derived from noise spectral density) and a low NEP of 1.02×10^{-12} W Hz$^{-1/2}$.

3 Transport layer design for low-noise OPDs

The transport layer facilitates the efficient extraction and transfer of charge carriers generated within the active layer of an OPD while simultaneously suppressing unwanted charge injection from the electrodes.[20,40,87] It also functions as a buffer layer that prevents direct contact between the active layer and electrodes, thereby alleviating interfacial defects and improving morphological quality.[88] Depending on its role, the transport layer can be classified as either an electron blocking layer (EBL), also referred to as a hole transport layer (HTL), or a hole blocking layer (HBL), also known as an electron transport layer (ETL). The specific functionality of each layer is governed by its HOMO and lowest unoccupied molecular orbital (LUMO) energy levels relative to those of adjacent layers. This section reviews key studies in which the judicious selection and engineering of transport layer materials have realized substantial reductions in dark current and noise in OPD devices.

3.1 EBL engineering for interface passivation

Due to the inherently low-current operation of OPDs, defects and energetic disorder at the EBL interface can elevate the overall noise level, severely limiting detectivity and critically impairing device performance. Therefore, recent studies have shifted their focus beyond merely enhancing the hole transport properties to emphasize strategies that leverage the electronic and chemical stability of the EBL to suppress interfacial defects and induce trap passivation, ultimately minimizing noise and maximizing detectivity.[89–92] In this context, EBL interface engineering and diverse processing methodologies have emerged as vital approaches for improving the photodetection capabilities of OPDs. This section provides a comprehensive overview of key studies demonstrating the suppression of interfacial noise through advanced EBL engineering.

Self-assembled monolayers (SAMs) have demonstrated wide applicability as EBLs in OPDs because of their high optical transparency, ability to tune the ITO work function, and minimal thickness.[93–97] The formation of an ordered monolayer *via* adsorption onto the electrode with anchoring groups, passivates the surface trap states and improves the film surface quality through controlled interfacial nucleation.[98,99] This reduces the interfacial trap states and leakage paths, providing a critical contribution to noise suppression. Kim *et al.* introduced the ((2,7-dibromo-9*H*-fluorene-9,9-diyl)bis(propane-3,1-diyl))diphosphonic acid (3PAFBr) SAM-based EBL to modulate the interfacial energy barrier between the EBL and active layer.[100] The 3PAFBr molecule features two phosphonic acid (PA) groups that enable strong adsorption onto the ITO electrode surface *via* bidentate or tridentate coordination. As shown in Fig. 7a, the extensive substitution of hydroxyl groups with P–O–M bonds reflects the strong adsorption efficiency of the dual-PA anchoring groups. This robust chemisorption passivates the trap states and suppresses the leakage current. Fig. 7b compares the R_{sh} values for different devices: the 3PAFBr-based OPD exhibited an exceptionally high R_{sh} value of 21.4 TΩ compared to R_{sh} values of 121 GΩ for Si photodetector (SiPD), 113.0 GΩ for a 2PACz-based OPD, and 4.52 GΩ for a poly(3,4-ethylenedioxythiophene) (PEDOT:PSS)-based OPD. According to eqn (4), an elevated shunt resistance will reduce the thermally agitated carrier motion, thereby lowering the thermal noise. As a result, the 3PAFBr device achieved a median I_{rms} value of 852 aA (Fig. 7c), representing the lowest noise current ever recorded in OPDs and confirming the outstanding noise suppression capabilities of this device. Oh *et al.* further advanced this approach by applying ((2,7-dicyano-9*H*-fluorene-9,9-diyl)bis(propane-3,1-diyl))bis(phosphonic acid) (3PAFCN) as an EBL to achieve an ultralow i_n and ultrahigh D^* in the NIR region, enabling single-pixel imaging under low-light and foggy conditions.[101] Similar to 3PAFBr, 3PAFCN contains two PA groups that strongly chemisorb onto the ITO surface and thereby impart a high surface energy. This

 This journal is © The Royal Society of Chemistry 2025

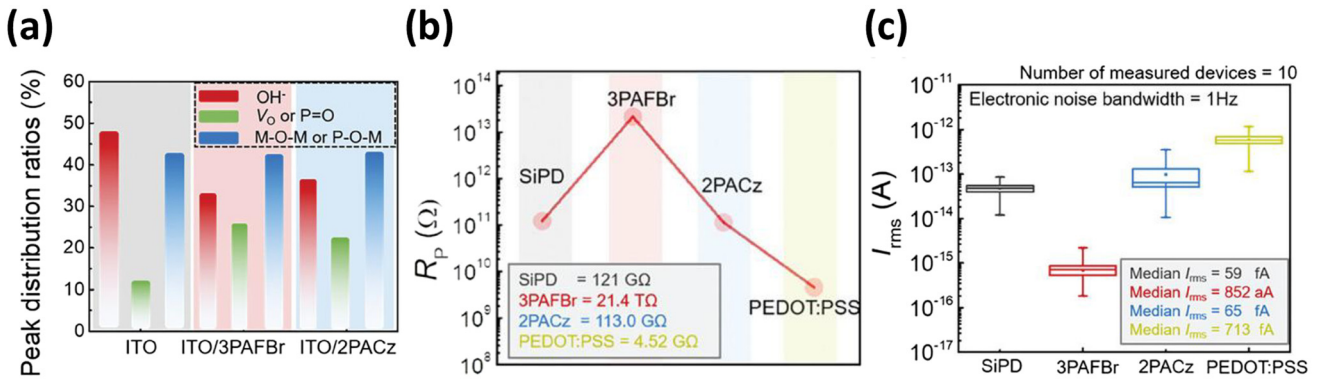

Fig. 7 (a) Comparison of peak areas based on oxygen peak deconvolution from XPS spectra. (b) Shunt resistance of SiPD and OPDs employing 3PAFBr, 2PACz, and PEDOT:PSS SAM EBLs. (c) Repeated measurements of noise current (I_{rms}). Reprinted with permission from ref. 100. Copyright © 2025, Wiley-VCH.

Published on 18 September 2025. Downloaded on 16.05.26 11:55:54.

not only promotes the heterogeneous nucleation of the Y6 acceptor, yielding finely dispersed domains that promote exciton dissociation, but also forms edge-on-oriented PM6 at the photoactive layer surface, which suppresses undesired hole-transport.[102,103] As shown in Fig. 8a, the activation energy (E_a) for the 3PAFCN-based OPD was 1.19 eV, significantly higher than that of the 2PACz-based device (0.79 eV). This increase was attributed to a larger interfacial barrier height (ϕ_B), defined as $\phi_B = E_{LUMO,Y6} - E_{HOMO,EBL}$, indicating enhanced suppression of thermally activated charge transport at the acceptor/EBL interface, as illustrated in Fig. 8b. Moreover, drive-level capacitance profiling (DLCP) measurements revealed reduced trap density at both the EBL/BHJ and BHJ/HBL interfaces in the 3PAFCN device compared with those in the 2PACz device, further validating the trap passivation effect (Fig. 8c and d). These combined features enabled the realization of ultrahigh D^* NIR OPDs capable of performing robust single-pixel imaging under diverse environmental conditions.

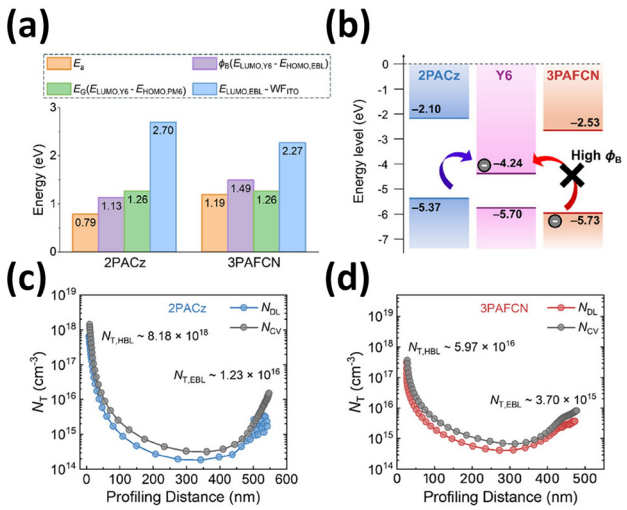

Fig. 8 (a) Values of E_a compared with various intrinsic potential energy levels. (b) Schematic of energy modulation suppression of electron thermal excitation. DLCP and C–V measurements of (c) 2PACz and (d) 3PAFCN OPDs. Reprinted with permission from ref. 101. Copyright © 2025, Wiley-VCH.

Several studies have explored the use of conjugated polymers, which were originally developed as donor materials, as EBLs to enhance OPD performance.[104] Xiong *et al.* employed P3HT, a conjugated polymer characterized by favorable energy level alignment and high hole mobility, as an EBL using a transfer-printing technique to effectively suppress dark current under reverse bias conditions.[105] Under this approach, poly(dimethylsiloxane) (PDMS) was used as the transfer medium to laminate a P3HT film onto the active layer, enabling the fabrication of inverted-structure OPDs. The detailed P3HT transfer process is illustrated in Fig. 9a. This method circumvents the solvent nonorthogonality issue typically encountered when spin-coating, in which the solvent in the P3HT solution disrupts the morphology of the underlying active layer. The transfer-printed P3HT layer forms a compact film that minimizes pinhole formation and prevents direct contact between the active layer and anode, thereby reducing the leakage current (Fig. 9b). As shown in Fig. 9c, the noise current in the P3HT-based device exhibited frequency-independent behavior, indicating negligible contributions from both flicker and g–r noise. Given that flicker noise is primarily associated with charge trapping, this result confirms the low trap density of the P3HT EBL OPDs. The reduction of flicker and g–r noise lowers low-frequency noise and enhances D^*.

3.2 HBL modification for defect suppression

While HBLs share fundamentally equivalent mechanisms as EBLs, their material choice limitation typically to metal oxides has given rise to distinct noise suppression strategies associated to oxide-based interfaces. In particular, solution-processed oxide HBLs contain defects such as oxygen vacancies and pinholes that serve as charge-trapping centers and leakage pathways, thereby elevating the noise level. Therefore, recent research has focused on chemically controlling these defects and tailoring interfacial properties to lower the noise

Published on 18 September 2025. Downloaded on 16.05.26 11:55:54.

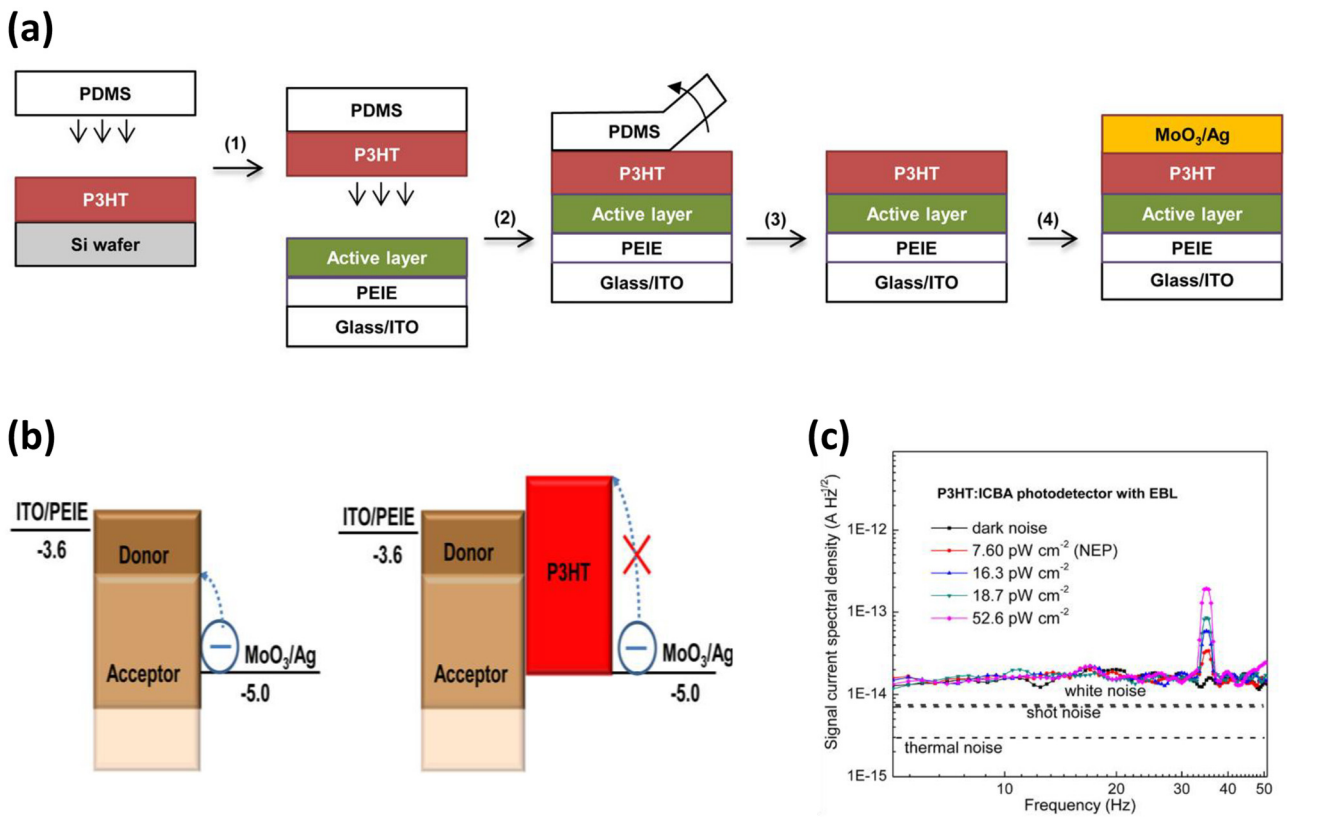

Fig. 9 (a) Fabrication steps and structure of OPDs incorporating a transfer-printed P3HT EBL: (1) P3HT film transferred from Si wafer to PDMS; (2) PDMS/P3HT laminated onto glass/ITO/PEIE/active layer; (3) PDMS peeled off, leaving P3HT; (4) top electrode deposition completed the device. (b) Schematic showing the P3HT layer blocking electron injection under reverse bias. (c) Noise current of OPD-P3HT w/EBL under 525 nm illumination at various light intensities. Reprinted with permission from ref. 105. Copyright © 2017, American Chemical Society.

floor.[106–108] This approach is gaining attention as an essential strategy for next-generation applications requiring high sensitivity, low-noise operations.

Notably, ZnO is among the most widely used HBL materials in OPDs because of its high electron mobility, excellent optical transparency, and compatibility with solution processing.[109,110] However, ZnO intrinsically contains oxygen vacancies (V_O) that serve as the origins of both shallow and deep trap states and lead to an increased dark current and degraded SNR.[111] Jang *et al.* addressed this issue by introducing alcohol-soluble tetraphenylethylene (TPE) to passivate the oxide vacancies chemically and thereby suppress trap-assisted recombination and shunt leakage.[112] The TPE-4 molecule contains four sulfonate (R-SO_3^-) chains that insert into the V_O sites, filling the defects and reducing trap density. Measurements obtained by X-ray photoelectron spectroscopy (XPS) shown in Fig. 10a–c, indicated a decrease in the V_O peak intensity from 73.2% in neat ZnO to 58.7% in the ZnO/TPE-4 film, confirming the successful passivation of surface vacancies with sulfonate ions. From an electronic transport perspective, the incorporation of TPE-4 suppressed unfavorable charge injection and reduced the dark current. The valence band energies of ZnO and ZnO/TPE-4 were determined to be −6.97 eV and −7.58 eV, respectively, and the corresponding conduction band energies were −4.06 eV and −3.68 eV. The deeper valence band and shallower conduction band of the modified film increased the hole injection barrier and reduced hole injection from the ITO electrode. This energy alignment decreased the dark current and thereby reduced shot noise, enhancing D^*. Lim *et al.* used a complementary approach to demonstrate that light exposure can effectively passivate V_O, improve surface morphology, and suppress the leakage current.[113] Fig. 11 presents atomic force microscopy (AFM) images and peak-to-valley data for pristine and light-exposed ZnO/PM6:Y6 films. The surface roughness of the pristine sample, initially measured at 8.016 nm, was reduced to 5.061 nm after light treatment, indicating that oxygen-related surface defects were effectively mitigated to produce a smoother film. Together, these two studies underscore the potential value of chemically modulating the intrinsic defects in ZnO to enhance its performance in low-noise OPDs, further establishing this material as a strong candidate for HBLs. Huang *et al.* employed a ZnO:PDINO hybrid HBL, formed by incorporating PDINO into sol–gel ZnO, to address the intrinsic limitations of ZnO.[114] PDINO molecules passivate oxygen vacancies present on the surface and within the bulk of the ZnO film, thereby eliminating charge tunneling pathways. In addition, the ZnO:PDINO hybrid HBL reduces the work func-

 This journal is © The Royal Society of Chemistry 2025

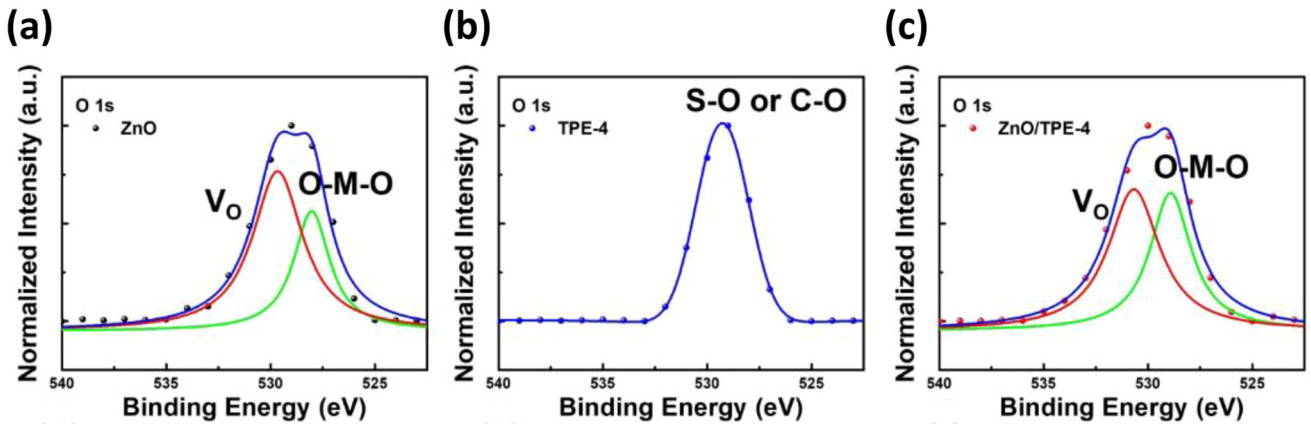

Fig. 10 XPS analysis of the O 1s regions of the (a) ZnO layer, (b) TPE-4 buffer layer, and (c) ZnO/TPE-4. Reprinted with permission from ref. 112. Copyright © 2023, Elsevier.

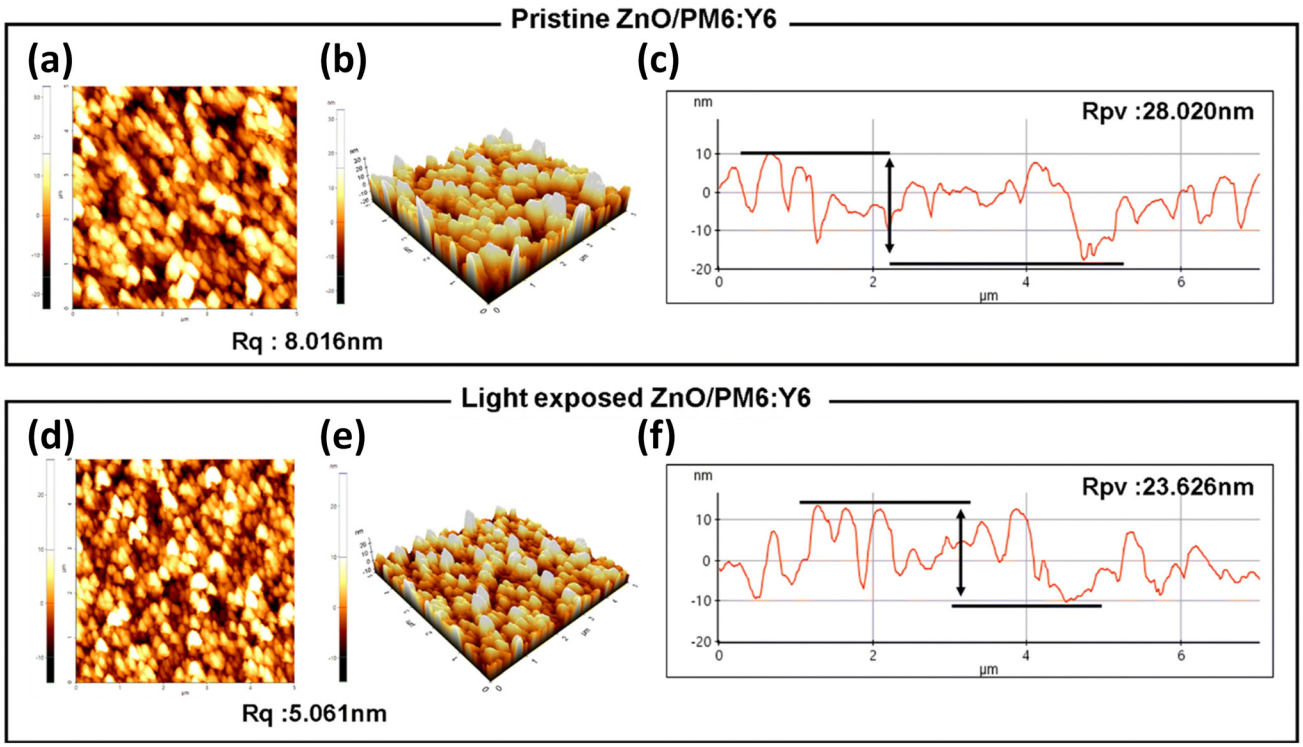

Fig. 11 2D and 3D AFM topography and peak-to-valley analysis of (a–c) the pristine ZnO/PM6:Y6 films, and (d–f) ZnO/PM6:Y6 films after 15 minutes of light exposure. Reprinted with permission from ref. 113. Copyright © 2023, Royal Society of Chemistry.

tion of ITO by approximately 0.11 eV, which increases the injection barrier, suppresses injection current, and consequently lowers the shot-noise floor. The high conductivity of PDINO further reduces device capacitance, mitigating interfacial charge accumulation, which in turn increases shunt resistance and decreases thermal noise. As a result, the white-noise-current-based detectivity measured in the 100–1000 Hz range reaches a high value of 1.09×10^{12} Jones at 1000 nm, a performance enhancement directly attributable to the suppression of white noise achieved by the hybrid HBL.

Huang *et al.* improved OPD stability under UV exposure by utilizing SnO_2 as an HBL to prevent surface oxygen desorption, a phenomenon known to degrade performance and elevate noise.[115,116] The wide optical bandgap of SnO_2 (4.35 eV, as shown in Fig. 12a) effectively minimizes UV absorption and suppresses UV-induced surface degradation. Additionally, SnO_2 forms an accumulation layer composed of adsorbed water molecules that contributes to its intrinsic environmental stability.[117] The structural integrity of the OPD is enhanced by employing a double-layer SnO_2 HBL, which improves blockage

Published on 18 September 2025. Downloaded on 16.05.26 11:55:54.

Published on 18 September 2025. Downloaded on 16.05.26 11:55:54.

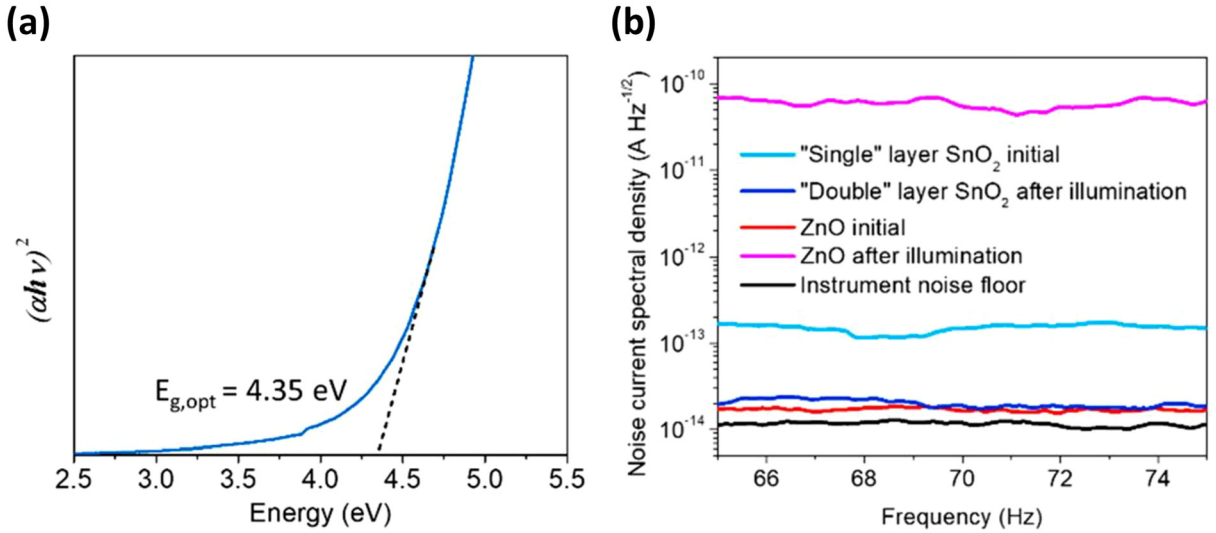

Fig. 12 (a) Tauc plot of SnO_2 film. (b) Noise spectral density of OPDs with SnO_2 and ZnO HBLs before and after illumination. Reprinted with permission from ref. 115. Copyright © 2021, American Chemical Society.

of hole injection and reduces pinhole formation. As shown in Fig. 12b, this optimized configuration maintained an extremely low noise level close to the noise floor even after prolonged UV illumination, highlighting its effectiveness in preserving low-noise operation under harsh optical stress.

4 Innovations in OPD architecture

The innovation of OPD architecture has emerged as a promising strategy for overcoming the limitations of conventional single-junction OPD configurations, enabling advanced functionalities and improving scalability.[118] This section focuses on photomultiplication-type OPDs (PM-OPDs) and tandem OPD architectures accordingly. The former are designed to achieve high R through internal charge amplification, whereas the latter enable multispectral detection by extending the photon absorption range across multiple stacked subcells.[119,120] In both architectures, the enhancement of the SNR, suppression of noise, and improvement in detectivity are critical for achieving application-specific performance goals such as improved linearity and operational stability during photocurrent amplification as well as maximized sensitivity in designated spectral regions. The functional capabilities realized through these architectural innovations and various detectivity enhancement strategies are discussed in this section.

4.1 Noise-suppressed PM-OPDs with internal gain

Representing class of functional OPDs, PM-OPDs are capable of achieving EQE that significantly exceed 100% by utilizing internal gain mechanisms to amplify photogenerated charges.[121–123] This amplification arises from trap-assisted carrier accumulation at the interface, which induces energy-band bending and facilitates carrier tunneling from the electrode, thereby enhancing the photocurrent and maximizing R.[124–128] However, as discussed in the Introduction, strategies that solely prioritize R often encounter trade-offs, particularly owing to nonlinearity in the photo-responses at low- and high-powered optical illumination levels and under elevated dark current. Therefore, balancing R and dark current to optimize detectivity is critical. Kublitski *et al.* demonstrated that identifying the optimum operating bias can help to balance this trade-off and realize high D^* PM-OPDs.[129] The core gain mechanism of their proposed design involves electron accumulation in the 3 wt% low-acceptor content C_{60} region, which creates a strong internal electric field that facilitates hole injection and induces a substantial tunneling current. Fig. 13a compares the current density–voltage (J–V) characteristics of the proposed PM-OPDs and a reference pin-photodiodes under dark and 100 mW cm^{-2} illumination, indicating an optimal bias condition at −2.5 V that suppressed dark current while maximizing the photocurrent. As a result, the PM-OPDs achieved superior detectivity compared to the pin structure, as illustrated in Fig. 13b. In a separate study, Xing *et al.* fabricated vacuum-processed PM-OPDs and successfully demonstrated the bias-independent D^* values.[130] These devices were constructed by inducing carrier amplification through hole accumulation in the BDP-OMe:C_{60} active layer, which had a low donor content of 4 wt%, to promote electron injection (Fig. 13d). The use of n-doped HATNA-Cl_6 with a deep HOMO energy level established a formidable injection barrier that effectively suppressed hole injection under dark flat-band conditions, as shown in Fig. 13c. The D^* for this device was calculated using the following equation:

$$D^* = \frac{q\lambda \mathrm{EQE}}{hcS_{\mathrm{n,white}}} (\mathrm{cm\,Hz^{1/2}\,W^{-1}\ or\ Jones}) \quad (9)$$

where λ is the wavelength, h is Planck's constant, and c is the speed of light. The noise spectral density $S_{\mathrm{n,white}}$ for frequency-independent noise is defined as:

 This journal is © The Royal Society of Chemistry 2025

Published on 18 September 2025. Downloaded on 16.05.26 11:55:54.

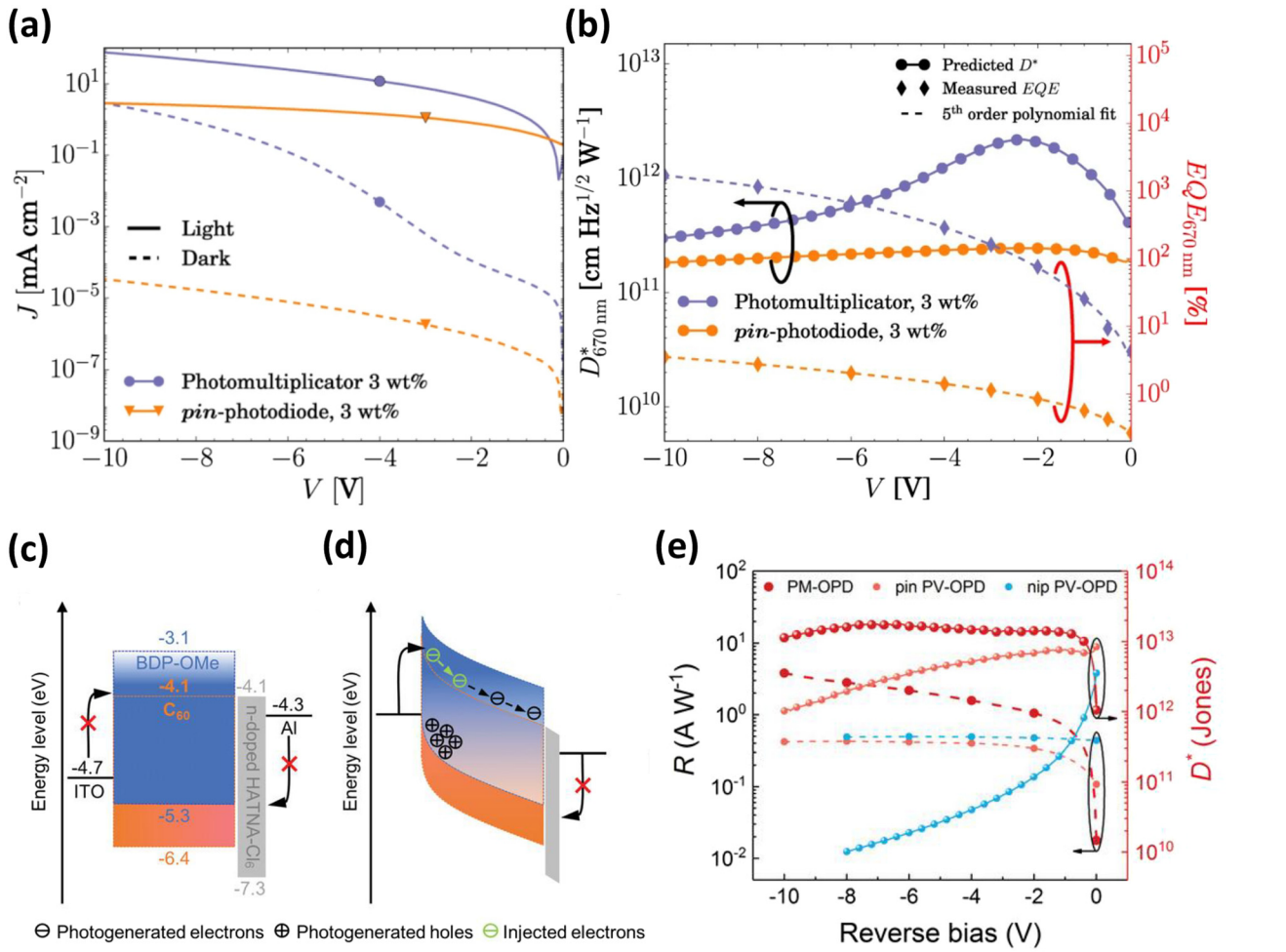

Fig. 13 (a) Dark and illuminated (100 mW cm^{-2}) *J*–*V* curves for a PM-OPD and pin photodiode (3 wt%). (b) Predicted detectivity and measured EQE at 670 nm for a PM-OPD and pin-photodiode (3 wt%) as a function of bias voltage. Reprinted with permission from ref. 129. Energy level diagrams of PM-OPDs: (c) in the dark under flat-band condition, and (d) under reverse bias with illumination. (e) Responsivity and shot-noise-limited *D* versus* reverse bias for PM-OPD, pin PV-OPD, and nip PV-OPD. Reprinted with permission from ref. 130.

$$S_{\mathrm{n,white}} = \sqrt{2qJ_{\mathrm{d}} + \frac{4k_{\mathrm{B}}T}{R_{\mathrm{sh,norm}}}}\ (\mathrm{A\,cm^{-1}\,Hz^{-1/2}}) \qquad (10)$$

where J_{d} is the dark current density. In this study, $R_{\mathrm{sh,norm}}$ is defined as the shunt resistance normalized by the area (Ω cm^2). Using eqn (9) and (10), the voltage-dependent D^* was plotted based on the fitted EQE at 780 nm, as shown in Fig. 13e. Although the resulting D^* values tended to be overestimated owing to the exclusion of frequency-dependent noise components, they successfully demonstrated the feasibility of high-performance, bias-independent PM-OPDs in the NIR regime, highlighting the potential for the future development of this architecture.

4.2 Tandem OPDs for broadband detection with noise mitigation

Tandem OPDs comprise multiple photo-detecting subcells that are vertically stacked to achieve broad spectral absorption as well as a high response speed and sensitivity.[120,131] As this multilayered architecture is inherently prone to generating interfacial noise, architectural innovations targeting a low dark current are essential. Liu *et al.* developed a tandem configuration combining a visible-light device (Poly([2,6′-4,8-di(5-ethylhexylthienyl)benzo[1,2-*b*;3,3-*b*]dithiophene]{3-fluoro-2[(2-ethylhexyl)carbonyl]thieno[3,4-*b*]thiophenediyl}) (PTB7-Th): 2,2′-[[6,6,12,12-Tetrakis(4-hexylphenyl)-6,12-dihydrodithieno[2,3-*d*:2′,3′-*d*′]-*s*-indaceno[1,2-*b*:5,6-*b*′]dithiophene-2,8-diyl]bis[methylidyne(3-oxo-1*H*-indene-2,1(3*H*)-diylidene)]]bis[propanedinitrile] (ITIC)) with a NIR device (PTB7-Th:FOIC) to enable the precise detection of light across the 300–1000 nm range with significantly reduced noise.[132] The working principle of this tandem structure is illustrated in Fig. 14a. Under a reverse bias, the applied voltage is divided across the two serially connected n–i–p junctions, effectively suppressing the reverse charge injection at each individual subcell and thereby reducing the dark current. The internal recombination region incorporates a MoO_x/Ag/polyethyleneimine ethoxylated (PEIE) interlayer in which the MoO_x and PEIE respectively act as p- and n-type

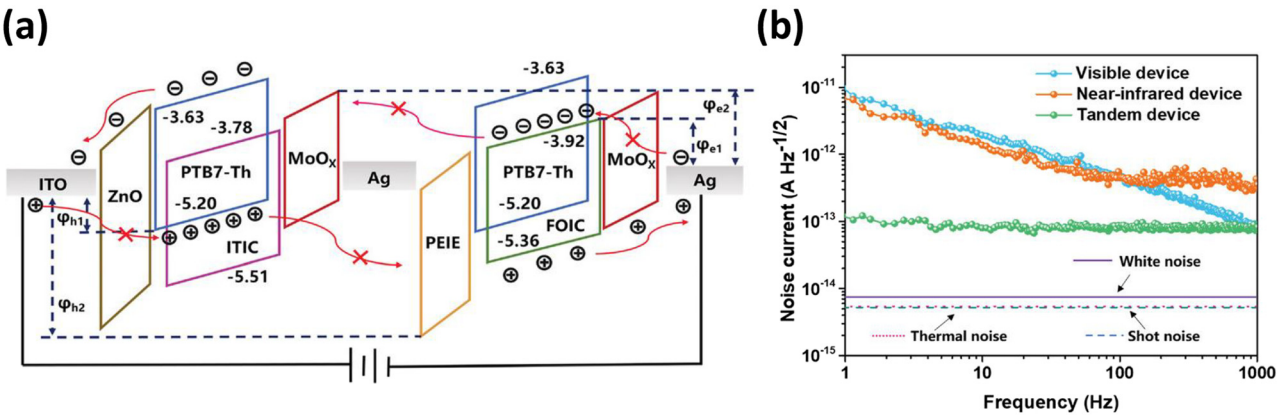

Fig. 14 (a) Schematic representation of the operating mechanism of the tandem device. (b) Noise currents of single-junction and tandem devices at a bias voltage of −0.1 V. Reprinted with permission from ref. 132. Copyright © 2021, Wiley-VCH.

Published on 18 September 2025. Downloaded on 16.05.26 11:55:54.

components and function as carrier-selective blocking layers.[133,134] This dual-barrier structure effectively minimizes injection-driven shot noise by restricting undesired charge-flow pathways. As shown in Fig. 14b, this tandem OPD exhibited lower overall noise than its single-junction counterparts constructed using the same materials while the flicker and g–r noise contributions remained negligible. These results indicate that the tandem OPD is a promising platform for suppressing injection and recombination noise while enabling high-fidelity, broadband photodetection.

5 Conclusion

Realizing OPDs with low noise and, consequently, high detectivity is a fundamental requirement for their emerging applications in fields such as optical communication and biosensing for which the detection of weak light signals is critical. However, under practical low-light conditions, OPDs face inherent limitations such as performance degradation caused by charge trapping–detrapping effects, ambient light fluctuations, and thermally generated carriers, making interface engineering and trap stabilization indispensable for overcoming these issues. Furthermore, in the NIR–SWIR region, where demand for next-generation applications is rapidly increasing, OPDs are fundamentally constrained by low bandgaps and limited absorption coefficients, which result in elevated noise levels and reduced optical efficiency. To address these challenges, innovative designs that integrate molecular and interfacial engineering are essential, enabling simultaneous extension of long-wavelength absorption, suppression of charge injection and trap states, preservation of responsivity, and minimization of NEP under real operating bandwidths, ultimately leading to enhanced D^*. Given that the detectivity of a photodetector quantitatively defines its sensitivity, this review adopted a device-level perspective to articulate the rationale for prioritizing noise suppression over maximizing responsivity as an effective strategy for performance enhancement. Building on this rationale, this review presented the underlying physical mechanisms responsible for various noise sources in OPDs. To suppress noise and enhance D^*, recent research trends have highlighted material strategies such as SAM-based EBLs, hybrid transport layers, and asymmetric non-fullerene acceptors, which simultaneously provide trap passivation and energy level alignment. The discussion focused on improved methods for device fabrication in terms of active and transport layer engineering as well as architectural innovations in device design. The systematic analysis of these approaches presented in this review provides a forward-looking roadmap for the continued development of next-generation OPDs with enhanced sensitivity.

Author contributions

S. Hong: investigation, conceptualization, writing – original draft. T. H. Kim: conceptualization, review & editing. S. Oh: review & editing. J. W. Shim: review & editing, supervision, funding acquisition.

Conflicts of interest

There are no conflicts to declare.

Data availability

No primary research results, software or code have been included and no new data were generated or analysed as part of this review.

Acknowledgements

This work was supported by the Technology Innovation Program (RS-2024-00404389, Development of low-power infra-

 This journal is © The Royal Society of Chemistry 2025

Published on 18 September 2025. Downloaded on 16.05.26 11:55:54.

red gas sensor technology for measuring various complex gases for a smart next-generation environment) funded By the Ministry of Trade, Industry, & Energy (MOTIE, Korea). In addition, this work was supported by the National Research Foundation of Korea (NRF) grant funded by the Korea government (MSIT) (No. 2022R1A2C2009523).

References

1 Y. Xia, J. Zhang, T. Guo, H. Wang, C. Geng, Y. Zhu, R. Han, Y. Yang, G. Song and X. Wan, *Adv. Funct. Mater.*, 2025, **35**, 2412813.
2 S. Cho, C. J. Heo, Y. Lim, S. Oh, D. Minami, M. Yu, H. Chun, S. Yun, H. Seo and F. Fang, *Adv. Sci.*, 2022, **9**, 2203715.
3 H. Jinno, T. Yokota, M. Koizumi, W. Yukita, M. Saito, I. Osaka, K. Fukuda and T. Someya, *Nat. Commun.*, 2021, **12**, 2234.
4 T. Yan, Z. Li, F. Cao, J. Chen, L. Wu and X. Fang, *Adv. Mater.*, 2022, **34**, 2201303.
5 R. D. J. Vuuren, A. Armin, A. K. Pandey, P. L. Burn and P. Meredith, *Adv. Mater.*, 2016, **28**, 4766–4802.
6 B. Yin, X. Zhou, Y. Li, G. Hu, W. Wei, M. Yang, S. Jeong, W. Deng, B. Wu and Y. Cao, *Adv. Mater.*, 2024, **36**, 2310811.
7 N. Huo and G. Konstantatos, *Adv. Mater.*, 2018, **30**, 1801164.
8 J. Liu, M. Gao, J. Kim, Z. Zhou, D. S. Chung, H. Yin and L. Ye, *Mater. Today*, 2021, **51**, 475–503.
9 M. Lim, X. Ma, Y. Kang, M. H. Jee, S. Lee, S. Y. Jeong, T. H. Kim, J. W. Shim, F. Zhang and H. Y. Woo, *Chem. Eng. J.*, 2025, **504**, 158769.
10 J. Wang, Z. Liu, T. Zhu, Z. Kang, X. Zeng, B. Zhou, Y. Zhou, J. Mu and Z. Yin, *Nano Energy*, 2024, **132**, 110399.
11 Y. Kang, T. H. Kim, M. J. Lee and J. W. Shim, *Small*, 2025, DOI: **10.1002/smll.202503701**.
12 H. Ren, J. D. Chen, Y. Q. Li and J. X. Tang, *Adv. Sci.*, 2020, **8**, 2002418.
13 S. Kim, S. J. Kim, G. Ham, J.-E. Jeong, D. Lee, E. Lee, H. Ahn, H. Cha, J. W. Shim and W. Lee, *J. Mater. Chem. A*, 2024, **12**, 2685–2696.
14 C. Labanti, J. Wu, J. Shin, S. Limbu, S. Yun, F. Fang, S. Y. Park, C. J. Heo, Y. Lim, T. Choi, H. J. Kim, H. Hong, B. Choi, K. B. Park, J. R. Durrant and J. S. Kim, *Nat. Commun.*, 2022, **13**, 3745.
15 S. Alam, S. Sim, M. Q. Li, S. Yang, J. Lee and J. Lee, *Mater. Today Chem.*, 2025, **46**, 102718.
16 Y. Wang, J. Kublitski, S. Xing, F. Dollinger, D. Spoltore, J. Benduhn and K. Leo, *Mater. Horiz.*, 2022, **9**, 220–251.
17 G. Suthar, C. W. Chu and F. C. Chen, *Adv. Opt. Mater.*, 2024, **12**, 2400662.
18 C. Fuentes-Hernandez, W.-F. Chou, T. M. Khan, L. Diniz, J. Lukens, F. A. Larrain, V. A. Rodriguez-Toro and B. Kippelen, *Science*, 2020, **370**, 698–701.
19 D. Yang and D. Ma, *Adv. Opt. Mater.*, 2018, **7**, 1800522.
20 T. Shan, X. Hou, X. Yin and X. Guo, *Front. Optoelectron.*, 2022, **15**, 49.
21 Y. K. Choi, T. H. Kim, B. K. Jung, T. Park, Y. M. Lee, S. Oh, H. J. Choi, J. Park, S. I. Bae and Y. Lee, *Small*, 2024, **20**, 2308375.
22 O. J. Sandberg, C. Kaiser, S. Zeiske, N. Zarrabi, S. Gielen, W. Maes, K. Vandewal, P. Meredith and A. Armin, *Nat. Photonics*, 2023, **17**, 368–374.
23 H. Wang, S. Xing, Y. Zheng, J. Kong, J. Yu and A. D. Taylor, *ACS Appl. Mater. Interfaces*, 2018, **10**, 3856–3864.
24 G. Simone, M. J. Dyson, S. C. Meskers, R. A. Janssen and G. H. Gelinck, *Adv. Funct. Mater.*, 2020, **30**, 1904205.
25 W. Wang, L. Shi, Y. Zhang, G. Li, Y. Hao, F. Zhu, K. Wang and Y. Cui, *Org. Electron.*, 2019, **68**, 56–62.
26 Z. Zhao, J. Wang, C. Xu, K. Yang, F. Zhao, K. Wang, X. Zhang and F. Zhang, *J. Phys. Chem. Lett.*, 2019, **11**, 366–373.
27 T. H. Kim, S. Y. Jeong, S. Oh, Y. Kang, M. J. Lee, M. H. Jee, H. Y. Woo and J. W. Shim, *Adv. Mater.*, 2025, 2500126.
28 E. Manna, T. Xiao, J. Shinar and R. Shinar, *Electronics*, 2015, **4**, 688–722.
29 Z. Yang, B. G. Kim, W. Jang and D. H. Wang, *J. Mater. Chem. C*, 2024, **12**, 3261–3271.
30 Q. Liu, S. Zeiske, X. Jiang, D. Desta, S. Mertens, S. Gielen, R. Shanivarasanthe, H.-G. Boyen, A. Armin and K. Vandewal, *Nat. Commun.*, 2022, **13**, 5194.
31 S. Zhang, T. Liu, J. Wang, Y. Li, G. Lin, M. Vasilopoulou, J. Chu, Q. Meng and X. Bao, *Adv. Opt. Mater.*, 2024, **12**, 2400328.
32 M. Kielar, O. Dhez, G. Pecastaings, A. Curutchet and L. Hirsch, *Sci. Rep.*, 2016, **6**, 39201.
33 Y.-Y. Yu, Y.-C. Peng, Y.-C. Chiu, S.-J. Liu and C.-P. Chen, *Nanomaterials*, 2022, **12**, 1378.
34 Y. Park, C. Fuentes-Hernandez, K. Kim, W.-F. Chou, F. A. Larrain, S. Graham, O. N. Pierron and B. Kippelen, *Sci. Adv.*, 2021, **7**, eabj6565.
35 H. Anabestani, S. Nabavi and S. Bhadra, *Nanomaterials*, 2022, **12**, 3775.
36 S. Gielen, C. Kaiser, F. Verstraeten, J. Kublitski, J. Benduhn, D. Spoltore, P. Verstappen, W. Maes, P. Meredith, A. Armin and K. Vandewal, *Adv. Mater.*, 2020, **32**, 2003818.
37 S. D. S. Rao, M. Jensen, L. Grüner-Nielsen, J. T. Olsen, P. Heiduschka, B. Kemper, J. Schnekenburger, M. Glud, M. Mogensen and N. M. Israelsen, *Light:Sci. Appl.*, 2021, **10**, 133.
38 A. Gover, A. Nause, E. Dyunin and M. Fedurin, *Nat. Phys.*, 2012, **8**, 877–880.
39 D. Baierl, L. Pancheri, M. Schmidt, D. Stoppa, G.-F. D. Betta, G. Scarpa and P. Lugli, *Nat. Commun.*, 2012, **3**, 1175.
40 Z. Lan, M.-H. Lee and F. Zhu, *Adv. Intell. Syst.*, 2022, **4**, 2100167.
41 Y. Fang and J. Huang, *Adv. Mater.*, 2015, **27**, 2804–2810.

Published on 18 September 2025. Downloaded on 16.05.26 11:55:54.

42 X. Jia, Q. Wei, Y. Zhu and W. Zhang, *AIP Adv.*, 2024, **14**, 095212.
43 T. Martin and R. Landauer, *Phys. Rev. B: Condens. Matter Mater. Phys.*, 1992, **45**, 1742.
44 J. Liang, H. Wang, Z. Yin, M. Jia, M. Wang, D. Yan, X. Hou and J. Zhang, *J. Mater. Chem. C*, 2025, **13**, 3917–3926.
45 C. Lin, Y. Su, S. Chang, H. Huang, S. Chang and T. Sun, *IEEE Photonics Technol. Lett.*, 2002, **9**, 232–234.
46 X. Ma, R. A. Janssen and G. H. Gelinck, *Adv. Mater. Technol.*, 2023, **8**, 2300234.
47 V. Mitin, L. Reggiani and L. Varani, in *Noise and Fluctuations Control in Electronic Devices*, ed. A. Balandin, American Scientific Publishers, California, 1st edn, 2002, ch. 2, pp. 2–20.
48 Y. Xia, L. E. Aguirre, X. Xu and O. Inganäs, *Adv. Electron. Mater.*, 2020, **6**, 1901017.
49 T. Kleinpenning, S. Jarrix and G. Lecoy, *J. Appl. Phys.*, 1995, **78**, 2883–2885.
50 J. Glemža, V. Palenskis, S. Pralgauskaitė, J. Vyšniauskas and J. Matukas, *Infrared Phys. Technol.*, 2018, **91**, 101–106.
51 X. Zhao, J. Wang, M. Liu, X. Ma and F. Zhang, *Adv. Opt. Mater.*, 2024, **12**, 2401087.
52 Y. Li, H. Chen and J. Zhang, *Nanomaterials*, 2021, **11**, 1404.
53 Q. Eynaud, A. Khodr, M. E. A. Kramdi, G. Quéléver, O. Margeat, J. Ackermann and C. Videlot-Ackermann, *J. Appl. Polym. Sci.*, 2024, **141**, e55481.
54 G. Yang, Z. Wang, Y. Duan, D. Zhao and J. Yu, *Nanoscale Res. Lett.*, 2019, **14**, 201.
55 H. T. Chandran, C. Yan and G. Li, *Adv. Energy Sustainability Res.*, 2022, **3**, 2200002.
56 W. Zhong, X. Wang, W. Wang, Z. Song, Y. Tang, B. Chen, T. Yang and Y. Liang, *Adv. Sci.*, 2025, **12**, 2410332.
57 M. H. Jee, B. Park, A. Y. Lee, S. Rhee, M. Lim, J. M. Ha, N. Kim, F. Zhang, J. W. Ha and H. Ahn, *Chem. Eng. J.*, 2024, **490**, 151624.
58 H. Quan, Z. Zhong, T. Hao, K. An, W. Zhong, C. Wang, F. Liu, L. Ying and F. Huang, *Chem. Eng. J.*, 2023, **452**, 139295.
59 M. Rimmele, Z. Qiao, F. Aniés, A. V. Marsh, A. Yazmaciyan, G. Harrison, S. Fatayer, N. Gasparini and M. Heeney, *ACS Mater. Lett.*, 2024, **6**, 5006–5015.
60 H. J. Eun, H. Kye, D. Kim, I. S. Jin, J. W. Jung, S.-J. Ko, J. Heo, B.-G. Kim and J. H. Kim, *ACS Appl. Mater. Interfaces*, 2021, **13**, 11144–11150.
61 T. Zhang, J. Schröder, J. Wolansky, K. Leo and J. Benduhn, *Appl. Phys. Lett.*, 2024, **124**, 193502.
62 R. Butkute, A. Masiulyte, E. U. Rashid, S. Sargsyan, N. S. Moudgalya, K. Leitonas, D. Volyniuk and J. V. Grazulevicius, *ACS Appl. Electron. Mater.*, 2024, **6**, 4735–4745.
63 B. H. Jiang, Y. Y. Hsu, Y. W. Su, S. F. Peng, Z. E. Shi and C. P. Chen, *Adv. Opt. Mater.*, 2025, **13**, 2500258.
64 K. Cho, J. W. Ha, M. Nam, C. Lee, S. J. You, A. Y. Lee, S. C. Yoon, M. Han, J. H. Kim and S. J. Ko, *Adv. Funct. Mater.*, 2024, **34**, 2400676.
65 C. Labanti, Y. Sun, J. Luke, Y. Dong, S. Y. Park, Y. C. Chin, T. Lan, E. J. Yang, L. Zhang, S. Gonzalez-Carrero, J. R. Durrant and J. S. Kim, *Adv. Opt. Mater.*, 2025, **13**, 2500255.
66 Y. Gao, J. Liao, H. Chen, H. Ning, Q. Wu, Z. Li, Z. Wang, X. Zhang, M. Shao and Y. Yu, *Adv. Sci.*, 2023, **10**, 2204727.
67 S. Y. Park, C. Labanti, R. A. Pacalaj, T. H. Lee, Y. Dong, Y. C. Chin, J. Luke, G. Ryu, D. Minami and S. Yun, *Adv. Mater.*, 2023, **35**, 2306655.
68 J. Luke, E. J. Yang, Y. C. Chin, Y. Che, L. Winkler, D. Whatling, C. Labanti, S. Y. Park and J. S. Kim, *Adv. Energy Mater.*, 2022, **12**, 2201267.
69 Y. Li, D. Zhao, D. Zhang, M. Wu, Y. Liu and J. Yu, *Opt. Lett.*, 2022, **47**, 3375–3378.
70 S. Xiong, J. Li, J. Peng, X. Dong, F. Qin, W. Wang, L. Sun, Y. Xu, Q. Lin and Y. Zhou, *Adv. Opt. Mater.*, 2022, **10**, 2101837.
71 M. He, J. Han, C. Li, C. Han, X. Han, X. Du, H. Luo, H. Yu, J. Gou, Z. Wu and J. Wang, *Laser Photonics Rev.*, 2024, **19**, 2400554.
72 S. J. Kim, M. A. Saeed, T. H. Kim, G. Ham, H. Song, H. Ahn, H. Choi, J. W. Jo, Y. Kim and H. Cha, *Chem. Eng. J.*, 2024, **488**, 151154.
73 J. Huang, J. Lee, J. Vollbrecht, V. V. Brus, A. L. Dixon, D. X. Cao, Z. Zhu, Z. Du, H. Wang and K. Cho, *Adv. Mater.*, 2020, **32**, 1906027.
74 W. Jang, H. M. Luong, M. S. Kim, T. Q. Nguyen and D. H. Wang, *Adv. Mater.*, 2024, **36**, 2406316.
75 G. M. Lee, T. H. Kim, G. Ham, M. J. Lee, S. Oh, Y. Kang, H. Ahn, H. Cha, S. Chung and J. W. Shim, *ACS Nano*, 2025, **19**, 4650–4662.
76 M. J. Lee, T. H. Kim, S. H. Lee, S. Oh, M. A. Khan, G. M. Lee, Y. K. Choi, S. Lee, H. Ahn and S. J. Oh, *Adv. Funct. Mater.*, 2025, **35**, 2421080.
77 C. Michelson, A. Gelatos and J. Cohen, *Appl. Phys. Lett.*, 1985, **47**, 412–414.
78 Z. Ni, S. Xu and J. Huang, *Science*, 2021, **371**, eabd8598.
79 C. Xu, P. Liu, C. Feng, Z. He and Y. Cao, *J. Mater. Chem. C*, 2022, **10**, 5787–5796.
80 Y. Zhu, H. Chen, R. Han, H. Qin, Z. Yao, H. Liu, Y. Ma, X. Wan, G. Li and Y. Chen, *Natl. Sci. Rev.*, 2024, **11**, nwad311.
81 Z. Wu, N. Li, N. Eedugurala, J. D. Azoulay, D.-S. Leem and T. N. Ng, *npj Flexible Electron.*, 2020, **4**, 6.
82 U. H. Lee, B. Park, S. Rhee, J. W. Ha, D. R. Whang, H. J. Eun, J. H. Kim, Y. Shim, J. Heo and C. Lee, *Adv. Opt. Mater.*, 2023, **11**, 2300312.
83 T. Bills, C. T. Liu, J. Lim, N. Eedugurala, P. Mahalingavelar, B. Seo, E. T. Hanna, T. N. Ng and J. D. Azoulay, *Adv. Funct. Mater.*, 2024, **34**, 2314210.
84 J. Kublitski, A. Hofacker, B. K. Boroujeni, J. Benduhn, V. C. Nikolis, C. Kaiser, D. Spoltore, H. Kleemann, A. Fischer, F. Ellinger, K. Vandewal and K. Leo, *Nat. Commun.*, 2021, **12**, 551.
85 J. Cong, Z.-H. Huang, S.-W. Liu, Z. Luo, F.-Z. Liu, Z. Chen, K.-M. Lee, Y.-C. Huang and C. Yang, *Small*, 2025, **21**, 2410418.

 This journal is © The Royal Society of Chemistry 2025

Published on 18 September 2025. Downloaded on 16.05.26 11:55:54.

86 J.-W. Ha, A. Y. Lee, H. J. Eun, J.-H. Kim, H. Ahn, S. Park, C. Lee, D. W. Seo, J. Heo, S. C. Yoon, S.-J. Ko and J. H. Kim, *ACS Nano*, 2023, **17**, 18792–18804.
87 W. Yang, W. Qiu, E. Georgitzikis, E. Simoen, J. Serron, J. Lee, I. Lieberman, D. Cheyns, P. Malinowski and J. Genoe, *ACS Appl. Mater. Interfaces*, 2021, **13**, 16766–16774.
88 B. Farhadi, M. Ciprian, F. Zabihi and A. Liu, *Sol. Energy*, 2021, **226**, 161–172.
89 H. M. Luong, S. Chae, A. Yi, J. Chatsirisupachai, B. M. Kim, Y. Wan, V. Promarak, H. J. Kim and T.-Q. Nguyen, *Matter*, 2024, **7**, 2473–2489.
90 K. Lu, Y. Gao, Z. Wang, X. Wang and H. Meng, *J. Mater. Chem. C*, 2023, **11**, 8600–8608.
91 A. Grimoldi, L. Colella, L. La Monaca, G. Azzellino, M. Caironi, C. Bertarelli, D. Natali and M. Sampietro, *Org. Electron.*, 2016, **36**, 29–34.
92 C. Xu, K. Miao, F. Eisner, G. Liu, C. Feng, H. Su, L. Lan, Z. He and J. Nelson, *Adv. Opt. Mater.*, 2024, **12**, 2302555.
93 M. Li, M. Liu, F. Qi, F. R. Lin and A. K.-Y. Jen, *Chem. Rev.*, 2024, **124**, 2138–2204.
94 M. J. Lee, J.-S. Park, T. H. Kim, M. A. Saeed, G. M. Lee and J. W. Shim, *Chem. Eng. J.*, 2024, **481**, 148481.
95 Z. Li, Z. Chen, Z. Shi, G. Zou, L. Chu, X.-K. Chen, C. Zhang, S. K. So and H.-L. Yip, *Nat. Commun.*, 2023, **14**, 6441.
96 D. Li, Q. Lian, T. Du, R. Ma, H. Liu, Q. Liang, Y. Han, G. Mi, O. Peng and G. Zhang, *Nat. Commun.*, 2024, **15**, 7605.
97 M. Halik and A. Hirsch, *Adv. Mater.*, 2011, **23**, 2689–2695.
98 M. J. Lee, S. Oh, M. A. Saeed, Y. Kang, G. M. Lee, H. Ahn, Y. Kim and J. W. Shim, *IEEE Trans. Electron Devices*, 2024, **71**, 4723–4731.
99 S. Oh, Y. Kang, T. H. Kim, S. J. Kim, M. J. Lee, G. M. Lee, M. A. Saeed and J. W. Shim, *JPhys Energy*, 2024, **6**, 025015.
100 T. H. Kim, J. H. Lee, M. H. Jang, G. M. Lee, E. S. Shim, S. Oh, M. A. Saeed, M. J. Lee, B. S. Yu, D. K. Hwang, C. W. Park, S. Y. Lee, J. W. Jo and J. W. Shim, *Adv. Mater.*, 2024, **36**, 2403647.
101 S. Oh, S. Jo, J. H. Lee, H. W. Ko, T. H. Kim, P. H. Seo, G. M. Lee, E. S. Shim, H. Ahn, B. K. Jung, S. J. Oh, D. Park, K. H. Lee, S. K. Yoon, B. Chae, S. Lee, G. Y. Lee, J. W. Jo, S. Y. Lee, M. C. Park and J. W. Shim, *Adv. Mater.*, 2025, **37**, 2503868.
102 Y. Li, J. Ding, C. Liang, X. Zhang, J. Zhang, D. S. Jakob, B. Wang, X. Li, H. Zhang and L. Li, *Joule*, 2021, **5**, 3154–3168.
103 Y. Li, J. Wu, X. Yi, Z. Liu, H. Liu, Y. Fu, J. Liu and Z. Xie, *J. Mater. Chem. C*, 2023, **11**, 13263–13273.
104 T. H. Kim, Y. K. Choi, G. M. Lee, M. A. Saeed, B. K. Jung, M. J. Lee, H. J. Choi, S. J. Oh and J. W. Shim, *Adv. Mater.*, 2024, **36**, 2309028.
105 S. Xiong, L. Li, F. Qin, L. Mao, B. Luo, Y. Jiang, Z. Li, J. Huang and Y. Zhou, *ACS Appl. Mater. Interfaces*, 2017, **9**, 9176–9183.
106 T. Klab, B. Luszczynska, J. Ulanski, Q. Wei, G. Chen and Y. Zou, *Org. Electron.*, 2020, **77**, 105527.
107 J. Wang, S. Deng, J. Hu, J. Miao, J. Li, J. Liu and Y. Liu, *Adv. Funct. Mater.*, 2024, **34**, 2312502.
108 F.-C. Hsu, Z.-Y. Yeh and C.-P. Li, *J. Mater. Chem. C*, 2024, **12**, 14445–14454.
109 Z. Liang, Q. Zhang, L. Jiang and G. Cao, *Energy Environ. Sci.*, 2015, **8**, 3442–3476.
110 J. Huang, Z. Yin and Q. Zheng, *Energy Environ. Sci.*, 2011, **4**, 3861–3877.
111 T. J. Wijaya, S. Xiong, K. Sasaki, Y. Kato, K. Mori, M. Koizumi, S. Lee, M. Kobayashi, Y. Zhou and K. Fukuda, *Adv. Mater.*, 2025, **37**, 2501951.
112 W. Jang, Z. U. Rehman, M. Haris, J. S. Cho, J. Lim, M. S. Kim, J.-C. Lee, H. K. Lee and D. H. Wang, *Chem. Eng. J.*, 2023, **472**, 144847.
113 J. Lim, W. Jang, J. Lee, J. Y. Chun and D. H. Wang, *Inorg. Chem. Front.*, 2023, **10**, 2995–3006.
114 Y.-C. Huang, T.-Y. Wang, Z.-H. Huang and S. R. M. S. Santiago, *ACS Appl. Mater. Interfaces*, 2024, **16**, 27576–27586.
115 J. Huang, J. Lee, H. Nakayama, M. Schrock, D. X. Cao, K. Cho, G. C. Bazan and T. Q. Nguyen, *ACS Nano*, 2021, **15**, 1753–1763.
116 T. J. Wijaya, T. Yokota, S. Lee, R. Okano, M. Kobayashi and T. Someya, *Adv. Photonics Res.*, 2023, **4**, 2200355.
117 Y. Jiang, L. Sun, F. Jiang, C. Xie, L. Hu, X. Dong, F. Qin, T. Liu, L. Hu and X. Jiang, *Mater. Horiz.*, 2019, **6**, 1438–1443.
118 H. S. Kim, M. A. Saeed and J. W. Shim, *J. Power Sources*, 2024, **618**, 235179.
119 D. Guo, D. Yang, J. Zhao, A. Vadim and D. Ma, *J. Mater. Chem. C*, 2020, **8**, 9024–9031.
120 S. M. Menke, R. Pandey and R. J. Holmes, *Appl. Phys. Lett.*, 2012, **101**, 223301.
121 J. Wang and Q. Zheng, *J. Mater. Chem. C*, 2019, **7**, 1544–1550.
122 X. Zhao, K. Yang, X. Ma, M. H. Jee, H. Qu, S. Zhang, Y. Ma, L. Shen, G. Yuan and Q. Yao, *Chem. Eng. J.*, 2025, **517**, 164473.
123 X. Tang, L. Li, Y. Yang, X. Qiao and Y. Wang, *Opt. Lett.*, 2024, **49**, 6745–6748.
124 J. Miao and F. Zhang, *Laser Photonics Rev.*, 2019, **13**, 1800204.
125 Z. Zhao, C. Xu, L. Niu, X. Zhang and F. Zhang, *Laser Photonics Rev.*, 2020, **14**, 2000262.
126 L. Shi, Q. Liang, W. Wang, Y. Zhang, G. Li, T. Ji, Y. Hao and Y. Cui, *Nanomaterials*, 2018, **8**, 713.
127 W. Wang, F. Zhang, M. Du, L. Li, M. Zhang, K. Wang, Y. Wang, B. Hu, Y. Fang and J. Huang, *Nano Lett.*, 2017, **17**, 1995–2002.
128 S. Yoon, G. S. Lee, K. M. Sim, M. J. Kim, Y. H. Kim and D. S. Chung, *Adv. Funct. Mater.*, 2021, **31**, 2006448.
129 J. Kublitski, A. Fischer, S. Xing, L. Baisinger, E. Bittrich, D. Spoltore, J. Benduhn, K. Vandewal and K. Leo, *Nat. Commun.*, 2021, **12**, 4259.

Published on 18 September 2025. Downloaded on 16.05.26 11:55:54.

130 S. Xing, J. Kublitski, C. Hanisch, L. C. Winkler, T. Y. Li, H. Kleemann, J. Benduhn and K. Leo, *Adv. Sci.*, 2022, **9**, 2105113.
131 X. Zhang, J. Jiang, B. Feng, H. Song and L. Shen, *J. Mater. Chem. C*, 2023, **11**, 12453–12465.
132 J. Liu, J. Jiang, S. Wang, T. Li, X. Jing, Y. Liu, Y. Wang, H. Wen, M. Yao, X. Zhan and L. Shen, *Small*, 2021, **17**, 2101316.
133 Z. Tang, Z. Ma, A. Sánchez-Díaz, S. Ullbrich, Y. Liu, B. Siegmund, A. Mischok, K. Leo, M. Campoy-Quiles and W. Li, *Adv. Mater.*, 2017, **29**, 1702184.
134 W. Li, Y. Xu, X. Meng, Z. Xiao, R. Li, L. Jiang, L. Cui, M. Zheng, C. Liu and L. Ding, *Adv. Funct. Mater.*, 2019, **29**, 1808948.
135 Y. Chen, Y. Zheng, J. Wang, X. Zhao, G. Liu, Y. Lin, Y. Yang, L. Wang, Z. Tang, Y. Wang, Y. Fang, W. Zhang and X. Zhu, *Sci. Adv.*, 2024, **10**, eadm9631.
136 W. Guo, Y. Duan, W. Liu, X. Zhang, J. Gao, Z. You, Y. Jiang, Z. Ma, X. Zhan and Y. Liu, *CCS Chem.*, 2025, **7**, 1731–1744.
137 L. Shao, J. Yang, Y. Huang, Y. Cao, J. Jing, X. Qin, X. Yang, H. Tang, C. Liu, F. Huang and Y. Cao, *Chem. Mater.*, 2024, **36**, 5775–5787.
138 H. Xia, J. Zhang, T. Guo, H. Wang, C. Geng, Y. Zhu, R. Han, Y. Yang, G. Song, X. Wan, G. Li and Y. Chen, *Adv. Funct. Mater.*, 2025, **35**, 2412813.
139 S. Zhang, T. Liu, J. Wang, Y. Li, G. Lin, M. Vasilopoulou, J. Chu, Q. Meng and X. Bao, *Adv. Opt. Mater.*, 2024, **12**, 2400328.
140 Z. Qiao, Q. He, A. D. Scaccabarozzi, J. Panidi, A. Marsh, Y. Han, P. Jacoutot, D. Nodari, T. Zhang, A. Way, A. J. P. White, T. D. Anthopoulos, W. C. Tsoi, A. A. Bakulin, M. Heeney, Z. Fei and N. Gasparini, *J. Mater. Chem. C*, 2024, **12**, 5766–5775.
141 X. Yu, H. Lin, Z. He, X. Yao, X. Du, Z. Chen, G. Yang, C. Zheng and S. Tao, *Adv. Opt. Mater.*, 2024, **12**, 2302170.
142 Y. Zhang, Y. Yu, X. Liu, J. Miao, Y. Han, J. Liu and L. Wang, *Adv. Mater.*, 2023, **35**, 2211714.
143 T. Liu, Z. Jia, Y. Song, N. Yu, Q. Lin, C. Li, Y. Jia, H. Chen, S. Wang, Y. Wei, Y. Lin, F. Huang, Z. Tang, Y. Li, L. Meng and H. Huang, *Adv. Funct. Mater.*, 2023, **33**, 2301167.
144 H. Quan, Z. Zhong, Z. Zhou, X. Wu, C. Shi, Z. Fink, G. Zhou, Y. Shang, Z. Yin, A. Zhang, C. Wang, N. Li, W. Zhong, F. Huang and L. Ying, *Adv. Opt. Mater.*, 2024, **12**, 2400818.
145 Y. Wang, M. Li, R. Wang, H. Shi, F. Li, Y. Zhu, G. Li, W. Ni, Y. Chen, M. Li and Y. Geng, *ACS Appl. Mater. Interfaces*, 2025, **17**, 42162–42173.
146 B. Yin, X. Zhou, Y. Li, G. Hu, W. Wei, M. Yang, S. Jeong, W. Deng, B. Wu, Y. Cao, B. Huang, L. Pan, X. Yang, Z. Fu, Y. Fang, L. Shen, C. Yang, H. Wu, L. Lan, F. Huang, Y. Cao and C. Duan, *Adv. Mater.*, 2024, **36**, 2310811.
147 Y. Xia, C. Geng, X. Bi, M. Li, Y. Zhu, Z. Yao, X. Wan, G. Li and Y. Chen, *Adv. Opt. Mater.*, 2024, **12**, 2301518.
148 M. Yang, B. Yin, G. Hu, Y. Cao, S. Lu, Y. Chen, Y. He, X. Yang, B. Huang, J. Li, B. Wu, S. Pang, L. Shen, Y. Liang, H. Wu, L. Lan, G. Yu, F. Huang, Y. Cao and C. Duan, *Chem*, 2024, **10**, 1425–1444.

This journal is © The Royal Society of Chemistry 2025